Retrograde metasomatic effects on phase assemblages in an interlayered blueschist-greenschist sequence (Coastal Cordillera, Chile)

Ralf Halama[1,*], Matthias Konrad-Schmolke[1]

[1] Institute of Earth and Environmental Science, University of Potsdam, Karl-Liebknecht-Str. 24-25, 14476 Potsdam, Germany

* Corresponding author contact information:
Ralf Halama
University of Potsdam
Institute of Earth and Environmental Science
Karl-Liebknecht-Str. 24-25
14476 Potsdam
E-mail: rhalama@geo.uni-potsdam.de
Tel: +49-331-977-5783
Fax: +49-331-977-5700

Revised version, submitted to Lithos 21. November 2014

Abstract

Interlayered blueschists and greenschists of the Coastal Cordillera (Chile) are part of a Late Palaeozoic accretionary complex. They represent metavolcanic rocks with oceanic affinities based on predominantly OIB-type REE patterns and immobile trace element ratios. Both rock types have similar mineralogies, albeit with different mineral modal abundances. Amphibole is the major mafic mineral and varies compositionally from glaucophane to actinolite. The presence of glaucophane relicts as cores in zoned amphiboles in both blueschists and greenschists is evidence for a pervasive high-pressure metamorphic stage, indicating that tectonic juxtaposition is an unlikely explanation for the cm-dm scale interlayering. During exhumation, a retrograde greenschist-facies overprint stabilized chlorite + albite + winchitic/actinolitic amphibole + phengitic white mica ± epidote ± K-feldspar at 0.4±0.1 GPa. Geochemical variability can be partly ascribed to primary magmatic and partly to secondary metasomatic processes that occurred under greenschist-facies conditions. Isocon diagrams of several adjacent blueschist-greenschist pairs with similar protolith geochemistry were used to evaluate metasomatic changes due to retrograde fluid-rock interaction. The most important geochemical changes are depletion of Si and Na and addition of water in the greenschists compared to the blueschists. Transition metals and LILE are mobilized to varying degrees. The unsystematic deviations from magmatic fractionation trends suggest open system conditions and influx of an external fluid. Pseudosection and water isopleth calculations show that the rocks were dehydrating during most of their exhumation history and remained at water-saturated conditions. The mineralogical changes, in particular breakdown of blue amphibole and replacement by chlorite, albite and calcic/sodic-calcic amphibole, are the prime cause for the distinct coloring. Pseudo-binary phase diagrams were used as a means to link bulk rock geochemical variability to modal and chemical changes in the mineralogy. The geochemical changes induced by fluid-rock interaction are important in two ways: First, the bulk rock chemistry is altered, leading to the stabilization of higher modal proportions of

chlorite in the greenschists. Second, the retrograde overprint is a selective, layer-parallel fluid infiltration process, causing more intense greenschist-facies recrystallization in greenschist layers and therefore preferential preservation of blue amphibole in blueschist layers. Hence, the distinct colors were acquired by a combination of compositional variability, both primary magmatic and secondary metasomatic, and the different intensity of retrograde fluid infiltration.

Keywords:
Fluid-rock interaction, metasomatism, element mobility, pseudo-binary phase diagrams, Coastal Cordillera (Chile)

1. Introduction

Interlayered sequences of blueschists, greenschists and/or eclogites frequently occur in subduction-related metamorphic terranes, such as the Cycladic Islands, Greece (Bröcker 1990), the Franciscan Belt, California (Oh et al. 1991), the Tauern Window, Eastern Alps (Selverstone et al. 1992), and Brittany, France (Barrientos and Selverstone, 1993; El Korh et al., 2009). Three distinct processes are commonly invoked to explain these apparent metamorphic heterogeneities within single units: 1) Equilibration at distinct pressure-temperature (P-T) conditions and late-stage tectonic juxtaposition (Ridley, 1984; Pognante and Kienast, 1987; Bousquet, 2008), 2) Chemical differences in the protolith (Dungan et al., 1983; Oh et al., 1991; El-Shazly et al., 1997; Baziotis and Mposkos, 2011; Pattison, 2013), occasionally combined with variable pre-metamorphic fluid overprinting (Dungan et al., 1983; El Korh et al., 2013), and 3) Variable retrograde overprinting resulting from different degrees of fluid infiltration during exhumation (Schliestedt and Matthews, 1987; Barrientos and Selverstone, 1993; Bröcker, 1990). Complete metamorphic equilibration is often inhibited by slow reaction kinetics and slow diffusion, so that deformation has a catalytic effect on re-equilibration (Pognante and Kienast, 1987; Konrad-Schmolke et al., 2011). The bulk rock composition of the protolith may also be directly linked to subsequent fluid-induced overprinting during metamorphism because compositions that are prone to dehydration are also more likely to re-equilibrate during retrogression (Baziotis et al., 2009). Variable bulk compositions can even cause changes in the mineralogy that mimic the progression of assemblages that undergo a facies transition during their metamorphic evolution (Kahl and Schumacher, 2000).

It is important to understand the processes that cause the occurrence of metamorphic heterogeneities within single units because each explanation provides distinct information about the tectonometamorphic history of the unit (e.g. Pattison, 2013) and constraints about

element transport during metamorphism. The occurrence of blueschist-facies assemblages without low-pressure overprint is interpreted to reflect retracing of the prograde P-T path during exhumation and upward motion of tectonically imbricated slices (Ernst, 1988). In contrast, the overprinting by greenschist and/or epidote-amphibolite facies assemblages is thought to involve rapid, nearly isothermal decompression and an approximately adiabatic rise of the subduction complex as consequence of deceleration/cessation of the subduction underflow (Ernst, 1988; 2006). Baziotis and Mposkos (2011) could show that the preservation of peak metamorphic blueschist assemblages also depends on bulk rock composition. In their example, preservation is promoted in Fe-rich bulk compositions because dehydration ends earlier compared to relatively Fe-poor compositions (Baziotis and Mposkos, 2011). If distinct protolith compositions can be identified as major cause for metamorphic heterogeneities, these can be used to deduce pre-subduction tectonic settings and pre-metamorphic alteration processes (Becker et al., 2000; Bebout, 2007; John et al., 2010; Hyppolito et al., 2014). During high-pressure low-temperature (HP-LT) subduction zone metamorphism, rocks often retain the geochemical characteristics of their protoliths, including hydrothermal alteration before subduction (Dungan et al., 1983; Putlitz et al., 2000; El Korh et al., 2009; Halama et al., 2011; van der Straaten et al., 2012). Fluids are not only important during pre-metamorphic alteration, but they are particularly of interest during syn-metamorphic processes because they facilitate the attainment of equilibrium and are a key factor for the transport of elements in subduction zones. Hence, differences in the retrograde overprint and variable degrees of fluid infiltration during the metamorphic evolution of a rock provide crucial information about fluid release, fluid sources and element mobility during metasomatic processes and associated metamorphic reactions (Bebout and Barton, 1993; Halama et al., 2011; Marschall et al., 2009; Miller et al., 2009; Penniston-Dorland et al., 2010; van der Straaten et al. 2008; 2012). Fluids can be internally derived by dehydration or local dissolution (Heinrich, 1982; Widmer and Thompson, 2001; Wangen and Munz, 2004; Baziotis et al., 2009; Verlaguet et al., 2011) with

metamorphic mineral growth occurring by small-scale (mm-dm) diffusive mass transfer during closed-system conditions (Philippot and Selverstone, 1991; Kohn et al., 1993). Alternatively, fluids can be externally derived by large-scale advective mass transfer (Walther and Orville, 1982; Beitter et al., 2008; Bucholz and Ague, 2010). In the latter case, a significant geochemical variability can be generated in the metamorphic rocks by interaction with metasomatic fluids during high-pressure metamorphism (Halama et al., 2011) and such fluid-rock interaction has significant effects on interpretation of geochronological data (Glodny et al. 2002; 2008; Halama et al., 2014). Moreover, similarities in the geochemistry of the rehydrated rocks can be related to geochemical patterns in arc volcanic rocks and the direct examination of subduction zone metamorphic rocks provides insights about slab-derived agents added to arc magma sources in the mantle wedge (e.g. Sorensen et al., 1997; Breeding et al., 2004; El Korh et al., 2009; John et al., 2004; Spandler et al., 2004; Bebout, 2007; Beinlich et al., 2010; van der Straaten et al. 2008). In the context of interlayered rocks with apparently distinct metamorphic facies, it is important to note that syn-metamorphic compositional changes influence phase relations and phase compositions. As a result, spatial variations in the intensity of fluid-rock interaction and the amount of mass transfer may be more important for determining the rock's mineralogy than changes in P-T conditions (Goncalves et al., 2012). The effects of mass transfer, i.e. changes in composition due to metasomatic overprinting, can be explored through pseudosection thermobarometry (Goncalves et al., 2013; Evans et al., 2013).

This study investigates the causes of interlayering in a sequence of layered blueschists and greenschist from the Coastal Cordillera in Chile. The first major objective is the distinction between pre-subduction, inherited geochemical variability and elemental mobility during metamorphic fluid-rock interaction based on the systematic evaluation of geochemical differences between blueschists and greenschists in terms of pre- and syn-metamorphic processes. The second aim is to understand the effect of fluid-rock interaction on the

mineralogy of the rocks and the link between metasomatic overprint and retrogression by quantifying the phase relations and compositions as a function of bulk rock chemical transformations. We show that the interlayering of the investigated rocks results from compositional variations and is not due to tectonic juxtaposition because the rocks experienced the same P-T evolution. The compositional and mineralogical variations observed can be partly attributed to primary magmatic differences. For some blueschist-greenschist pairs, we are able to demonstrate that selective fluid infiltration in the greenschist facies caused different degrees of retrograde metasomatic overprinting.

2. Geological Setting

In the Coastal Cordillera of Chile, the crystalline basement of the Mesozoic and Cenozoic Andean sequences consists of metamorphic and associated magmatic rocks of Paleozoic to Triassic age (Hervé et al., 2007). Basement exposures in the Coastal Cordillera comprise fossil accretionary prisms, which are partly associated with a magmatic arc and high-temperature metamorphic belts (Hervé, 1988). Two units of this basement, the Western and the Eastern Series (Fig. 1), were recognized to constitute a classic Pacific-rim type paired metamorphic belt (Aguirre et al., 1972; Ernst, 1975). Geochronological studies in these units provided evidence for Late Paleozoic subduction along the western margin of South America (Munizaga et al., 1973; Hervé et al., 1974), corroborating the interpretation that the Western and Eastern Series constitute coeval parts of a Late Palaeozoic paired metamorphic belt (Willner, 2005).

Both, the Western and the Eastern Series, are dominated by metamorphosed and deformed siliciclastic sediments that represent former turbidite deposits. The Eastern Series comprise a very low-grade metapelite-metagreywacke sequence with minor calcsilicate rocks (Hervé,

1988; Willner et al., 2000), interpreted as frontally accreted sediments (Richter et al., 2007). Locally, the rocks of the Eastern Series experienced a thermal overprint at around 296-301 Ma at maximum temperatures of 720 °C (Willner, 2005) caused by the coeval Late Palaeozoic magmatic arc batholith formation (Willner, 2005; Hervé et al., 1988). In contrast to the Eastern Series, the Western Series comprise a mixture of continent-derived siliciclastic rocks and subordinate slices of dismembered upper oceanic crust. The metabasites of the oceanic crust, which partly exhibit relict pillow structures, form lenses of meter to kilometer size. Minor rock types associated with the metabasites include serpentinite, marble, metachert, black graphite-rich metapelite, and ferruginous metasediments with stilpnomelane (Hervé, 1988; Hervé et al., 2007; Hyppolito et al., 2014). Among the metabasites, greenschists are the most common rock type. They experienced peak P-T conditions of 0.70-0.93 GPa at 380-420 °C (Willner, 2005) and are interpreted to reflect conditions of basal accretion in the accretionary prism (Willner et al., 2009). Rare blueschists occur as lenses of 1-5 m thickness at only three locations within the Western Series, scattered over a distance of ~60 km. These blueschists yielded peak P-T conditions of 0.95-1.07 GPa and 350-385 °C (Willner, 2005), which are similar to those of the more typical greenschists. The blueschists are considered as fragments of the oceanic crust that were incorporated into the subduction channel (Willner, personal communication). Both, greenschists and blueschists, experienced a retrograde metamorphic stage at ~300-380 °C and ~0.4-0.8 GPa, indicating pressure release with little cooling (Willner, 2005).

A $^{40}Ar/^{39}Ar$ phengite plateau age of 292±2 Ma from a blueschist was interpreted as peak HP imprint coeval with the formation of the transposition foliation (Willner et al., 2005). Throughout the Western Series, variability in the timing of the HP event (292-319 Ma) is observed based on $^{40}Ar/^{39}Ar$ UV laser ablation phengite plateau ages (Willner et al., 2005). The HP event is coeval with the main pulse of late Paleozoic arc magmatism (~305 Ma, $^{207}Pb/^{206}Pb$ zircon evaporation). *In situ* $^{40}Ar/^{39}Ar$ analyses of phengite in microfolds yielded

an absolute age range from 257 to 321 Ma and are interpreted to record long-lasting recrystallization (up to ~40 Myr for individual samples) during retrograde pressure release, considering that there is no indication of a potential excess argon component on inverse isochron diagrams (Willner et al., 2005). A retrograde metamorphic stage was identified in various rock types and reflects a pressure release of 0.3-0.4 GPa accompanied by only slight cooling to 300-380 °C (Willner, 2005). Later magmatic activity in the Western Series is represented by isolated granite plutons with intrusion ages between 257 ($^{207}Pb/^{206}Pb$ zircon evaporation; Willner et al., 2005) and 220 Ma (Rb-Sr mineral isochron; Lucassen et al., 2004). Afterwards, the retreat of the subducting slab caused termination of accretionary processes.

At Infiernillo Beach in Pichilemu (34°23.35 S, 72°01.33 W; Fig. 1), strongly foliated blueschists occur interlayered with greenschists, producing a pronounced banding on the cm to dm scale (Fig. 2). The sequence is interpreted to comprise various metavolcanic rocks (metatuffs, meta-agglomerates and metalavas) that are associated with metasedimentary rocks (pelitic schists, graphite-rich metapelites and quartzites; Hyppolito et al., 2014). Willner (2005) described structures resembling hyaloclastites and suggested that the presence of white mica in metabasite may point to former tuffitic deposits. The layering is parallel to the main foliation, which has transposed an earlier foliation and the stratigraphic surface (Hyppolito et al., 2014). Hyppolito et al. (2014) provide a detailed outcrop description of Infiernillo Beach and an interpretation of geochemical data in terms of the geodynamic setting of protoliths and the regional terrane assembly in central Chile. Here, we concentrate on several selected blueschists and greenschists from this location in the context of retrograde metasomatic overprinting.

3. Methodology

3.1 Geochemistry

In total, 11 samples from the layered sequences were analyzed for bulk rock major and trace element contents. We selected three interlayered blueschist-greenschist pairs for detailed microscopic and mineral chemical analyses. These sample pairs were taken either in direct contact (<10 cm apart) in the outcrop (sample pair CH-1-18 and CH-1-19) or carefully cut using the rock saw (samples CH-1-12 and CH-1-15) to ensure an accurate separation of blue and green parts of individual pairs.

Major element compositions of rock-forming minerals were determined using a JEOL JXA 8900R electron microprobe at the University of Kiel, operated with 15 kV, a 15 nA beam current and a beam diameter of 5 μm. Measurement times were 15s on the peak and 7s on the background, except for Cl, which was measured 30s and 15s, respectively. Natural standards were used for calibration and a CITZAF matrix correction was applied.

Whole rock major element contents were analyzed by X-ray fluorescence (XRF) on fused glass discs with a Philips PW1480 XRF spectrometer at the University of Kiel. The relative standard deviation (RSD) for all oxides is generally ≤ 1.3% based on multiple analyses of reference material BHVO-1 (see van der Straaten et al., 2008, for details on precision and accuracy). Concentrations of 37 trace elements were determined by inductively coupled plasma mass spectrometry (ICP-MS), after HF-HNO_3-$HClO_4$ acid digestion in Teflon bombs at 180°C, using an Agilent 7500c instrument at the University of Kiel. Details of sample preparation and the analytical protocol are given in Garbe-Schönberg (1993) and John et al. (2008). Analyses of the reference material and representative duplicate analyses are given in Table 1, and data for the procedural blank analyzed during the course of this study are given in Halama et al. (2013). Instrumental precision, as determined by multiple analyses of one sample solution and expressed as relative standard deviation (RSD), is typically ≤1.5 % for most trace elements, including the REE and Th, and up to 4 % for Sc, Cr, Co, Ni, Ta and Hf.

3.2 Phase diagram calculations

Phase diagrams were calculated using version 6.6.6 of the Perple_X software package (Connolly, 1990, 2005) in the system CNKFMASHO (CaO-Na_2O-K_2O-FeO-MgO-Al_2O_3-SiO_2-H_2O-O_2). Pseudosection calculations were performed at 300-500 °C and 0.2-1.2 GPa for water-saturated conditions. The chemical potential of oxygen in the system was controlled by the hematite-magnetite (HM) buffer. The advantage of buffering the oxygen fugacity is that open-system processes can be investigated by assuming that the oxidation state is controlled by a metamorphic stable mineral paragenesis and not by the amount of oxygen brought in or removed from the system (Konrad-Schmolke et al., 2008; Scott et al., 2013). The HM buffer assemblage seems appropriate because hematite is present in several samples, indicating relatively oxidizing conditions. The P-T positions of water isopleths, showing the molar percentage of water bound to 100% solids, were superimposed on the calculated pseudosections to evaluate the hydration/dehydration behavior under closed-system conditions. Pseudo-binary P-X_{H2O} diagrams were calculated to compare calculated mineral assemblages and modal and chemical mineral variations in the two samples for water-saturated and water-undersaturated conditions. Moreover, we calculated pseudo-binary P-X diagrams, using the blueschist and greenschist bulk compositions as compositional end-members, to evaluate the dependence of modal mineralogy and mineral chemistry on the different bulk chemistries. For all calculations, we used the updated database from Holland and Powell (1998) and solution models from Fuhrman and Lindsley (1988) for feldspar and from Holland et al. (1998) for chlorite, potassic white mica, epidote, garnet and omphacite. For amphibole, we used the solution model "GlTrTsMr" of Massonne and Willner (2008), which is based on the four end-members glaucophane, tremolite, tschermakite and magnesio-riebeckite and considers the incorporation of ferric iron into amphibole. We chose this model because it was specifically developed to take into account the compositional constraints of amphiboles at low-grade, medium-to-high pressure conditions, such as Si contents close to 8

per formula unit (pfu) and an almost vacant A site (Massonne and Willner, 2008). These compositional features are also present in the investigated samples, and this improved amphibole solution model has been successfully used to simulate the expected amphibole compositions for metabasites at low-grade metamorphic conditions (Massonne and Willner, 2008). We did not consider the andradite and acmite components in garnet and omphacite, respectively.

4. Petrography

All of the three blueschist-greenschist pairs investigated in detail are fine-grained with matrix minerals typically between 5 and 50 µm and rarely exceeding 100 µm in size. Major mineral phases are amphibole (amph), phengitic white mica (phg), chlorite (chl), and albite (ab) with subordinate amounts of titanite, epidote, hematite, apatite and K-feldspar (Fig. 3). Zircon and rutile occur as rare accessory phases. The mineralogy of blueschist and greenschist layers is similar, but the modal proportions of the major mineral phases differ (Table 2). Blue, sodic amphibole is significantly more abundant (>10%) in the blueschists compared to the greenschists. The proportion of blue amphibole as to all amphibole present is about 30-50% in blueschists, whereas it is <5% in greenschists. Modal chlorite increases in the greenschists to about 20-40% compared to the adjacent blueschists (~10%). Proportions of phengite and albite are variable and K-feldspar is typically lacking in the blueschists.

The presence of glaucophane in blueschists and greenschists provides evidence for a high-pressure metamorphic stage that affected the whole sequence. Rare rutile in one of the blueschists also reflects a high-P metamorphic stage. In contrast, the typical greenschist-facies minerals albite and chlorite demonstrate recrystallization at lower pressures during

exhumation. Alkali feldspar also appears texturally as a late-stage phase, whereas phengite may have been crystallizing and re-crystallizing over a wide P-T range on the retrograde path.

5. Mineral chemistry

Mineral chemical data of the major mineral phases are given in the electronic appendix. The two feldspars are essentially pure albite (~$An_{0.002}Ab_{0.996}Or_{0.002}$) and K-feldspar (~$Ab_{0.02}Or_{0.98}$), respectively. White mica has Mg# (Mg# = Mg/(Mg+Fe^{2+})) of 0.54-0.75 and Na/(Na+K) ratios <0.4. Silica content in white mica varies widely, both within and between different samples, from 6.5 to 7.2 Si pfu. In chlorite, Si pfu is relatively constant (5.6-6.0), whereas Mg# ranges from 0.55 to 0.67. Individual samples have a very restricted range of chlorite compositions with a variation in Mg# ≤0.02.

Amphibole has very wide compositional range. Sodic, sodic-calcic and calcic compositions are present (allocation of amphibole names following Locock (2014) based on Leake et al. (1997)). The majority of amphiboles has close to 8 Si pfu, between 0.3 and 1.8 Na_B and Mg# (Mg# = Mg/(Mg+Fe_T)) of 0.48-0.75 (Fig. 4). These amphiboles can be classified as actinolites, winchites, ferri-winchites and glaucophanes and represent a compositional continuum (Fig. 4). In both blueschist and greenschist samples, glaucophane cores are overgrown by sodic-calcic or calcic amphibole (Fig. 3A-D). In some cases, however, glaucophane appears to be surrounding sodic-calcic amphibole (Fig. 3E). Rare Ti-rich ferropargasite with TiO_2 between 3.2 and 6.2 wt.% occurs in two samples (blueschist CH-1-18 and greenschist CH-1-19), constituting the innermost parts of larger amphibole grains (Fig. 3F). Based on its textural position and its Ti-rich composition, the Ti-rich ferropargasite most likely formed prior to subduction zone metamorphism and is considered as the only remnant of the pre-metamorphic evolution.

6. Major and trace element chemistry

The eleven analyzed blueschists and greenschists are very variable in their major element composition, encompassing ultramafic, mafic and intermediate compositions (Table 1). The range in SiO_2 (40-56 wt.%), MgO (5.3-14.5 wt.%), total iron as Fe_2O_3 ($Fe_2O_3^T$, 9.1-16.5 wt.%), CaO (2.7-10.0 wt.%) and Na_2O (1.5-6.1 wt.%) is particularly large. Among the trace elements, Sr (23-681 µg/g), Li (20-56 µg/g), the large ion lithophile elements (LILEs), such as Rb (13-164 µg/g) and Ba (170-1360 µg/g), as well as the transition metals Cr (80-850 µg/g) and Ni (60-380 µg/g) show a considerable range. Whole-rock abundances of rare earth elements (REE) are also highly variable (La = 4-34 µg/g; Yb = 1.0-2.6 µg/g), resulting in distinct chondrite-normalized (CN) REE patterns (Fig. 5) and ratios ($(La/Yb)_{CN}$ = 1.5-12.6, $(La/Sm)_{CN}$ = 0.9-2.7 and $(Gd/Yb)_{CN}$ = 1.9-4.6). Compared to typical oceanic basalts, the REE patterns of most samples resemble ocean island basalts (OIBs) but are quite distinct from normal mid-oceanic ridge basalt (N-MORB). In contrast to volcanic rocks from the Chilean Volcanic Front, the main differences are the tendency to higher absolute REE contents and the lack of a flattening HREE slope. In the Th/Yb vs. Nb/Yb diagram (Pearce, 2008), used to discriminate between oceanic basalts and subduction-related basalts, most samples broadly fall between the alkalic and tholeiitic OIB compositions (Fig. 6).

In adjacent blueschist-greenschist pairs, blueschist layers are typically enriched in SiO_2 and Na_2O and depleted in MgO, $Fe_2O_3^T$ and H_2O compared to the associated greenschist, whereas CaO and K_2O lack systematic relationships with respect to rock type. The sequence CH-1-48, comprising a blueschist layer sandwiched in between two greenschists with distinctly different hues (Fig. 2), exhibits significant compositional differences not only between blueschist and greenschists but also between the two greenschists (Table 1, Fig. 5). In contrast, the adjacent blueschists and greenschists of three pairs have very similar REE slopes

compared to the respective greenschist/blueschist counterpart (Fig. 5). Moreover, the blueschists of the two pairs CH-1-12 and CH-1-18/19 are indistinguishable in terms of their Th/Yb and Nb/Yb ratios from the corresponding greenschists.

7. Discussion

7.1. Protolith composition

For altered and metamorphosed magmatic rocks, ratios of trace elements that are considered as immobile during low-grade alteration and metamorphism (Pearce and Cann, 1973; Pearce, 2008) can be used to determine the protolith composition. The Th/Yb versus Nb/Yb diagram combines Th/Yb as geochemical proxy for crustal input (via subduction, crustal recycling or magma-crust interaction) and Nb/Yb as proxy for mantle source/melting variance (Pearce, 2008). All samples fall into the field of oceanic basalts and do not show elevated Th/Yb ratios and low Nb/Yb ratios that are typical for the arc-related magmatic rocks from the Chilean volcanic front (Jacques et al., 2013). Hence, we exclude a subduction-related origin and favor formation in an oceanic setting. Hyppolito et al. (2014) also noted the lack of a subduction signature in blueschists and greenschists from the Coastal Cordillera of central Chile and attributed the observed N-MORB, E-MORB and OIB signatures to an oceanic origin.

On outcrop scale, blueschists and greenschists are interlayered with metasedimentary rocks, and hence a contribution of sedimentary material, either as detritus during deposition or by incorporation during subduction, has to be evaluated. In the Th/Yb vs. Nb/Yb diagram (Fig. 6) Chilean trench sediments (Lucassen et al., 2010) with high Th/Yb and low Nb/Yb ratios are geochemically distinct from the analyzed samples. Therefore, we do not consider that

admixing of a sedimentary component was a significant process in affecting the whole rock geochemistry of the blueschists and greenschists.

The overall heterogeneity in REE patterns from N-MORB-like to alkalic OIB-like (Fig. 5) is evidence for chemically heterogeneous precursor rocks. Most samples, however, have strongly negative REE slopes and correspondingly high (>5) $(La/Yb)_{CN}$ ratios, pointing to an ocean island origin, consistent with relatively high Nb/Yb ratios (Fig. 6). The chemical heterogeneity in the metavolcanic rocks can be explained by an origin at a plume-influenced ridge (Hyppolito et al., 2014) or at seamounts (John et al., 2010). Both scenarios can produce the coexistence of chemically diverse meta-igneous rocks in HP subduction complexes. The presence of Ti-rich ferropargasite relicts provides further support for an origin as igneous oceanic lithosphere because similarly Ti-rich pargasitic amphibole has been observed in ocean-floor ultramafic-mafic plutonic suites (Arai et al., 1997). Texturally similar inclusions of hornblende in metamafic rocks from the Attic-Cycladic blueschist belt were also assigned to an early, pre-HP metamorphism stage (Baziotis et al., 2009). In the context of this study, the key observation is that the metavolcanic rocks exhibit primary geochemical differences related to their magmatic origin, which are determined based on the REE patterns and distinct immobile trace element ratios (Nb/Yb, Th/Yb). The sample sequence CH-1-48 (Figs. 2, 5) provides an example for geochemical inheritance from the pre-metamorphic precursor rocks. On the other hand, three adjacent blueschist-greenschist pairs (samples CH-1-12, CH-1-15 and CH-1-18/19) have almost identical REE patterns (Fig. 5) and similar key HFSE ratios (Fig. 6). Since these elemental features typically remain unchanged during subduction-related metamorphism and retrogression (El Korh et al., 2009; 2013; John et al., 2004; 2010), these sample pairs are considered to reflect geochemically similar protoliths and to be suitable for the evaluation of additional, secondary effects on the bulk rock geochemistry.

7.2. Effects of igneous differentiation processes

Pre-metamorphic major and trace element variations that may have been caused by magmatic processes are assessed by comparing general fractional crystallization trends to the blueschist-greenschist pairs (Fig. 7). Some features of the major element abundances of individual blueschist-greenschist pairs, such as higher Na_2O and lower MgO contents in the more SiO_2-rich samples, are broadly compatible with a fractional crystallization relationship. However, there is evidence that typical magmatic relationships between major elements are disturbed, both for the entire sample set and individual blueschist-greenschist pairs.

Features that are inconsistent with igneous differentiation trends of ocean island volcanic rocks include (Fig. 7): (i) For a given MgO content, several blueschists have significantly higher SiO_2 and Na_2O contents compared to the igneous fractionation trend (ii) One greenschist is displaced to very low SiO_2 and shows an unusual, extreme enrichment in FeO^T. (iii) The slopes that connect matching blueschist-greenschist pairs in SiO_2-MgO space are oblique to the differentiation trend. (iv) CaO is relatively depleted in all samples except one. (v) The positive correlation of K_2O and Rb with MgO for two pairs is opposite to the igneous differentiation trend. (vi) There is a general enrichment in Ni, whereas the Cr contents scatter unsystematically. (vii) The behavior of incompatible trace elements relative to major elements is also difficult to explain with fractional crystallization alone because the more SiO_2-rich blueschists have similar or lower Zr, La and U contents than the greenschists (Table 1), whereas higher contents of these elements would be expected if fractional crystallization alone were responsible for the chemical variations. To conclude, many of geochemical variations present require element mobilization subsequent to the magmatic/volcanic history.

7.3. Chemical differences due to fluid-rock interaction

If igneous differentiation cannot explain several of the major element features, seafloor alteration and subduction and/or exhumation-related metamorphic processes remain as factors for the metasomatic overprint. The three selected blueschist-greenschist pairs, which show no

or little primary magmatic geochemical differences based on similar REE patterns and HFSE ratios, have unsystematic major element variations, indicating that metasomatic changes affected the rocks subsequent to the magmatic history. Hydrothermal alteration of oceanic crust is often observed in HP terranes (e.g., Putlitz et al., 2000; Spandler et al., 2004; Halama et al., 2011; El Korh et al., 2013), and metasomatic processes specific for ocean floor alteration, such as rodingitization and spilitization, have also been observed (Li et al., 2004; Arghe et al., 2011; Halama et al., 2013). Regarding major elements, gains and losses during seafloor alteration are highly variable and uncertainties in their quantification are high (Staudigel, 2003). For instance, Na is lost during submarine glass alteration (Staudigel and Hart, 1983), but spilitization leads to an increase in Na (Arghe et al., 2011). Therefore, potential effects of pre-metamorphic seafloor alteration are evaluated based on trace element abundances and ratios in diagrams that discern between seafloor alteration and high-pressure metasomatic processes (Fig. 8; Bebout, 2007; 2014). Increasing degrees of seafloor alteration in basaltic oceanic crust cause Ba/Rb and Th/U ratios to strongly decrease and K/Th to strongly increase (Fig. 8). Importantly, these trends are distinct from those observed for high-pressure metasomatic alteration (Bebout, 2007; 2014). None of the samples investigated falls onto any of the seafloor alteration trends, suggesting that this process had a negligible influence on the whole rock compositions. Instead, the samples plot close to typical OIB compositions, as expected from their immobile trace element signatures, or along the metasomatic alteration trends that illustrate chemical changes during subduction metamorphism. In particular, the three blueschist-greenschist pairs with negligible magmatic geochemical differences show trends that are subparallel to the general metasomatic alteration trend (Fig. 8). The apparent lack of typical seafloor alteration trends suggests that any metasomatic alterations of the whole rock geochemistry are related to fluid-rock interaction during the subduction-related metamorphic evolution.

For illustrative purposes, the chemical variations between individual blueschist-greenschist pairs are shown in isocon diagrams (Fig. 9). Isocon diagrams (Grant, 1986; 2005) are used to quantify chemical changes during metasomatism, and they have been successfully applied in elucidating transformation of eclogite into epidote amphibolite (El-Shazly et al., 1997) and eclogite into blueschist (van der Straaten et al., 2012). For the graphic representation of isocon diagrams, altered compositions are plotted against an original composition. Elemental species that have remained immobile in the investigated process define the isocon, which is a straight line through the origin (Grant, 2005). Here, the isocon diagrams reflect the integrated chemical variations of the rock's entire evolution and we use them to visualize geochemical variations and the general patterns of elemental behavior rather than the quantification of metasomatic changes. Although it is unlikely that blueschist and greenschist of individual pairs had exactly the same precursor, the near-identical REE patterns of the three selected pairs allows an evaluation of secondary metasomatic changes superimposed onto the primary magmatic differences.

The isocon analysis is based on a set of selected "immobile" reference elements and robust isocons can be defined based on >10 trace elements for each blueschist-greenschist pair (Fig. 9). Based on petrographic observations, we assume that blueschists are the less overprinted equivalents to the greenschists. The following observations can be made independent from absolute concentrations in the rocks: (i) SiO_2, CaO and Na_2O are relatively depleted in the greenschists. As SiO_2 and Na_2O increase but CaO decreases during igneous differentiation, these combined effects must be related to the metasomatic overprint. (ii) Greenschists are enriched in H_2O, consistent with the assumption of more intense fluid-rock interaction. (iii) MgO, $Fe_2O_3^T$ and transition metals show variable behavior. The observed scatter is partly due to differences in degree of fractionation, but the strong relative enrichment of these elements in one greenschist (Fig. 9C) suggests metasomatic mobilization of transition metals, as observed in several other studies of metamorphic fluid overprinting (El Shazly et al., 1997;

van der Straaten et al., 2012) and presumably linked to interaction with ultramafic lithologies. (iv) The four LILE K, Ba, Rb and Cs follow a distinct, linear array in all three examples, and the slope of this linear array is distinct from the slope defined by the reference elements. These trends point to a mineralogical control by potassic white mica (Sorensen et al., 1997; Bebout et al., 2007) and are probably related to fluid equilibration with metasedimentary lithologies. In two cases (Fig. 9A, B), LILE were added during fluid infiltration together with H_2O, whereas in the third case (Fig. 9C), LILE were removed during fluid-rock interaction.

7.4. Pseudosections

The application of thermodynamic modeling to metasomatized rocks faces the difficulties that textures produced by fluid-rock interaction are difficult to distinguish from those caused by P-T changes and that the selection of equilibrated minerals may be hampered by the variability in the scale of mass transfer and equilibration (Goncalves et al., 2013). For the Pichilemu rocks, relict glaucophane cores in both blueschist and greenschist (Fig. 3) bear evidence for a high-pressure metamorphic stage of the whole sequence. The textural evidence suggests that glaucophane is not in equilibrium with albite and K-feldspar, pointing to a distinct retrograde metamorphic stage (see also Willner, 2005). To explore phase assemblage and compositional variations, we calculated pseudosections for the blueschist-greenschist pair CH-1-18 – CH-1-19. This sample pair was selected because of a distinct difference in visual appearance and negligible differences in REE abundances and patterns reflecting a similar igneous protolith. Key features observed for these two samples also occur in the pseudosections calculated for the two other sample pairs, so that showing the entire set of diagrams for all samples is deemed redundant. We assume that the rocks are water-saturated at peak conditions, which is likely if continuous dehydration occurred along the prograde path (Konrad-Schmolke et al., 2011). The pseudosections for the two samples show broadly similar topologies despite small differences in detail (Fig. 10A-B). At peak conditions of around 1.0±0.1 GPa and 400±20 °C,

494 the predicted equilibrium assemblage is chlorite + epidote + phengite + amphibole. Albite
495 becomes stable below about 0.5±0.1 GPa and is joined by K-feldspar at still lower pressures.
496 Maximum equilibration pressures during retrograde overprint are constrained by the presence
497 of albite to about 0.4-0.6 GPa. The presence of K-feldspar in the greenschist constrains P to <
498 0.5 GPa, whereas minimum pressures are approximately 0.25 GPa based on the presence of
499 phengite. Hence, the best estimate for the retrograde overprint is 0.4±0.1 GPa at ≤ 400°C.
500 These estimates are clearly below peak pressure estimates of up to 1.1 GPa for blueschists
501 from the region (Willner, 2005), demonstrating that incomplete greenschist-facies
502 equilibration occurred after peak P-T on the retrograde path during exhumation. These
503 findings are in accordance with a significant pressure release with only slight cooling during
504 the retrograde P-T evolution (Willner, 2005). Based on the geochemical evidence presented
505 earlier, we suggest that the retrograde overprint is associated with layer-parallel fluid
506 infiltration, causing the different degrees of metasomatism under greenschist-facies
507 conditions.
508
509 *7.5. Influence of water on mineral assemblages and compositions*
510 The amount of structurally bound water in minerals is critical for the formation and
511 preservation of mineral assemblages during metamorphism (Guiraud et al., 2001; Clarke et
512 al., 2006; Konrad-Schmolke et al., 2011). To examine the mineral assemblage evolution along
513 the retrograde P-T path, we contoured the pseudosections for H_2O content of the mineral
514 assemblage (Fig. 10 A-B). Moreover, we modeled isothermal (T = 400 °C) P-X_{H2O} pseudo-
515 binary phase diagrams to study the influence of water undersaturation and water infiltration
516 on mineral assemblages as well as modal and chemical mineral variations (Fig. 10 C-F).
517 The water isopleths patterns of the examined blueschist and greenschist are very similar,
518 showing a positive slope above about 0.4-0.6 GPa, i.e. for all phase assemblages where albite
519 is lacking (Fig. 10 A-B). In contrast, water isopleths have a negative slope where albite is

present in the calculated mineral assemblage. Along the retrograde P-T path of the blueschist-greenschist sequence, successively lower isopleths are encountered within the 4-phase assemblage field chlorite+epidote+phengite+amphibole. Hence, decompression from peak pressure would result in dehydration because the capability of the rock to retain water diminishes (cf. Heinrich, 1982; Guiraud et al., 2001). Consequently, water saturation during decompression is attained without external water influx. The rock would remain water-saturated until albite joins the stable paragenesis where it becomes water-undersaturated as all the available water will be incorporated into the hydrous solid phases, rendered possible by the significant increase in the modal chlorite abundance (Fig. 10 A-B).

As inferred from the water isopleth patterns, the rocks remain at or above the water saturation line during decompression until pressures < 0.4 GPa are reached (Fig. 10 C-D). The absence of garnet and omphacite and the presence of K-feldspar in the Pichilemu samples also suggest crystallization conditions at or near water saturation. Only where the water saturation curve has a negative slope, external water addition is required to maintain water saturation (see also Konrad-Schmolke et al., 2011). The modal abundances of both chlorite (Fig. 10 C-D) and amphibole (Fig. 10 E-F) are strongly dependent on the degree of water-undersaturation, increasing with increasing water amounts, but show only moderate changes in water-saturated regions. The amphibole composition shows distinct patterns for water-undersaturated and water-saturated conditions (Fig. 10 E-F). The glaucophane component strongly decreases with increasing water content and shows only minor pressure dependence at water-undersaturation. However, once water saturation is reached, the amphibole composition solely depends on pressure, with a significant decrease in glaucophane component below pressures of ~0.35 GPa, i.e. where two feldspars are coexisting.

In summary, water-saturated or water-oversaturated conditions on the retrograde P-T path and the near-isothermal decompression are reflected in extensive albite crystallization and the growth of sodic-calcic and calcic amphibole around glaucophane. The almost mylonitic

546 textures that reflect high strain also favor extensive recrystallization of the Pichilemu rocks on
547 the retrograde P-T path. Although these features do not necessarily require influx of external
548 water, they are certainly consistent with fluid influx during the final equilibration stage.
549 Moreover, the significant deviations from igneous differentiation trends for major elements
550 are inconsistent with a closed system evolution and point to the presence of an external
551 metasomatic fluid triggering the retrograde equilibration. Supportive evidence for fluid influx
552 comes from the sharp compositional boundaries between glaucophane cores and
553 winchite/actinolite overgrowths. The lack of a continuous compositional trend in individual
554 amphiboles suggests discontinuous growth, which can be explained by a distinct fluid influx
555 as observed in eclogite-facies rocks from the Sesia Zone (Konrad-Schmolke et al., 2011;
556 Halama et al., 2014).
557
558 *7.6. Bulk compositional effects on mineral assemblages and compositions*
559 Previous studies have highlighted the important role of the bulk rock chemistry on amphibole
560 chemistry in interlayered blueschists and greenschists. Maruyama et al. (1986) proposed that
561 higher Fe contents expand the glaucophane stability, as glaucophane-bearing layers with
562 higher Fe contents were described (Oberhänsli et al., 1978; Dungan et al., 1983). Other
563 chemical variables, such as lower MgO and higher Na/Ca ratios in blueschists have also been
564 invoked to explain blueschist-greenschist interlayering (Baziotis et al., 2009; Dungan et al.,
565 1983). Evidently, phase stabilities depend on a complex interplay of major element
566 abundances. To accommodate for the complete major elemental variation of the rocks, we
567 calculated pseudo-binary phase diagrams for the selected blueschist-greenschist pair in order
568 to evaluate the influence of bulk chemical properties on modal phase abundances and mineral
569 compositions.
570 Calculated modal phase changes show that the chlorite abundance increases towards the end-
571 member greenschist component (Fig. 11A), which can be related to the relative increase of

572 MgO compared to SiO_2. Modal amphibole contents are higher for the blueschist. Both of
573 these modeled features agree with the observed modal abundances and the restricted
574 occurrence of glaucophane in greenschist layers. Interestingly, the calculated glaucophane
575 component is higher for the greenschist composition at any given pressure, demonstrating that
576 the scarcity of glaucophane in the greenschist must be related to a more intense degree of
577 retrograde overprinting in the greenschist relative to the blueschist at low pressure where a
578 more Ca-rich amphibole becomes stable. The pseudo-binary phase diagrams demonstrate that
579 chemical variations in adjacent lithologies are the dominant factor in determining their
580 appearance as "blue" or "green", without the necessity to invoke distinct P-T equilibration
581 conditions. Chemical variations can be related to two main causes, both of which are observed
582 in the Pichilemu rocks: 1) Primary compositional differences, inherited from a pre-subduction
583 stage, as in the sequence CH-1-48 A-B-C, and 2) Compositional changes that are induced by
584 fluid infiltration, affecting distinct layers to different degrees, as observed in the sample pair
585 CH-1-18/19.
586 Besides major element compositional variations, the oxidation state of metamorphic rocks
587 influences the stable mineral parageneses (Konrad-Schmolke et al., 2008; Diener and Powell,
588 2010) and their dehydration behavior (Massonne and Willner, 2008). For blueschist-facies
589 and greenschist-facies rocks, the preferential uptake of ferric iron by both sodic amphibole
590 and epidote relative to actinolite, chlorite and lawsonite exerts the most significant
591 compositional effect (Evans, 1990). Hence, the field of epidote and glaucophane is largest for
592 compositions rich in Fe^{3+}, i.e. for relatively oxidizing conditions (Evans, 1990), and the
593 addition of ferric iron moves the glaucophane-in boundary down to lower pressures (Diener et
594 al., 2007). In the Pichilemu samples, sodic amphibole is the major host of ferric iron because
595 epidote is only a minor phase and omphacite and garnet are absent. Hence, more oxidized
596 conditions would result in a larger stability field of sodic amphibole. However, we have
597 relinquished a more detailed discussion about the effects of oxygen fugacity because of two

598 reasons: First, despite recent improvements in the formulation of mineral solid solutions that
599 consider incorporation of Fe^{3+} (e.g. Diener et al., 2007), present knowledge about
600 thermodynamic properties of Fe^{3+} end-members is still incomplete and large uncertainties
601 exist about the Fe^{3+} standard state data and for the parameters of the mathematical
602 formulation of solid solution data (Scott et al., 2013). Second, it is difficult to relate observed
603 to modeled data because of the inability of the electron microprobe to resolve Fe valence
604 (Scott et al., 2013) and because bulk rock values of Fe_2O_3 may not reflect the oxidation state
605 during the main metamorphic evolution and may be modified by superficial alteration (López-
606 Carmona et al., 2013).
607
608 *7.7. Pre-metamorphic variability versus metamorphic overprinting*
609 The alternating layering on a cm-to-dm scale, the lack of structural breaks between the
610 different layers and the similar mineralogy of blueschists and greenschists suggest that the
611 whole sequence experienced a similar P-T evolution. If there is an appropriate spread in
612 whole rock compositions, reflected by mineral chemical variations along the exchange vectors
613 $Fe^{3+}Al_{-1}$ and $Fe^{2+}Mg_{-1}$, blueschists and greenschists can coexist over a pressure range of at
614 least 0.3 GPa and 400 °C (Evans, 1990). However, the Pichilemu rocks show abundant
615 evidence for retrogression in both rock types: Presence of albite ± K-feldspar, overgrowth of
616 winchite/ferrowinchite around glaucophane and actinolite and chlorite as abundant matrix
617 minerals. These observations and the pressure estimate of 0.4±0.1 GPa based on
618 pseudosection modeling demonstrate that an early blueschist event was followed by variable
619 retrograde overprint in the greenschist facies.
620 For several layers, exemplified in the chemically very heterogeneous sequence CH-1-48
621 (Figs. 2, 5, 7), the interlayering is best explained by metamorphism of layered volcanic rocks
622 (tuffs and/or basaltic lava flows) of different composition. In addition to primary magmatic
623 compositional differences, some features of the interlayered sequence were acquired by syn-

metamorphic fluid overprinting. Interlayering of blueschists and greenschists on a cm scale may be due to heterogeneous alteration of pillow lavas and subsequent flattening during metamorphism (Dungan et al., 1983). If metabasite layers are pervasively altered prior to metamorphism, they are likely to show greater effects of retrogression because of enrichment in Na and H_2O (El Korh et al., 2013). In the Pichilemu sequence, there is little evidence of pre-metamorphic alteration based on trace element systematics (Fig. 8) and because the blueschists, which are relatively enriched in Na, are also less retrogressed.

The detailed investigation of several blueschist-greenschist pairs revealed continuous gradations from blueschist to greenschist facies mineralogies in parts of the interlayered sequence and the persistence of blueschist-facies relicts in all rock types, pointing to an important role of synmetamorphic fluid-rock interaction and incomplete re-equilibration during uplift. Bröcker (1990) and Barrientos and Selverstone (1993) suggested that the retrograde blueschist-to-greenschist transformation is catalyzed by the availability of synmetamorphic fluid as the rocks pass through the greenschist facies by a selective infiltration overprinting process. All of the Pichilemu rocks show evidence for retrograde infiltration, but the effects were different in individual layers. We interpret these features as channeled infiltration subparallel to pseudo-stratigraphic layering, most likely controlled by differences in permeability (Bröcker, 1990).

8. Conclusions

Interlayered blueschists and greenschists occur in a fossil accretionary prism in the Coastal Cordillera of Chile. Their close spatial association on a cm-to-dm scale and the lack of structural breaks in between the layers argue against a large-scale tectonic transport of rocks with different metamorphic facies. The geochemical differences between blueschist and greenschist layers involve primary magmatic and secondary metasomatic processes. The

primary differences reveal that the rocks had oceanic basalts with dominantly OIB and subordinately MORB affinities as protoliths. Glaucophane relicts occur in both blueschists and greenschists, recording a high-pressure metamorphic event. The metasomatic overprint occurred under greenschist-facies conditions during exhumation and affected the rocks to different degrees. Gradational contacts between blueschists and greenschists on hand specimen and thin section scale and the persistence of blueschist-facies minerals in both rock types point to a selective infiltration overprinting during retrogression. Selected blueschist-greenschist pairs with similar REE patterns and immobile trace element ratios were used to evaluate geochemical effects of metasomatic overprinting. Key features of the metasomatic event include addition of water and depletion of Si and Na in greenschists relative to blueschists, mobilization and non-systematic behavior of most major elements and transition metals, and concurrent mobilization trends for K, Ba, Rb and Cs. Pseudosection calculations constrain the final equilibration to about 0.4±0.1 GPa at T <400 °C. The array of water isopleths shows that the rocks were dehydrating for the major segments of the retrograde P-T path, in agreement with the water saturation required to explain the modal mineralogy. Influx of an additional, external fluid is nevertheless indicated based on the geochemical arguments. Pseudo-binary phase diagrams of the metasomatic rocks reveal that the different bulk rock geochemistry of blueschists and greenschists, related to element mobilization by the external fluid, is responsible for a higher modal abundance of chlorite in greenschists. The second effect of the retrograde fluid-rock interaction is the preferential preservation of glaucophane in blueschists caused by a less intense overprint compared to the greenschists. Hence, layer-parallel, selective fluid infiltration is a key factor for the distinct visual appearance.

Acknowledgments

We appreciate in particular the advice and information provided by Arne Willner about the general geology of the Coastal Cordillera as well as about specific outcrop locations. We also thank M. Büscher, I. Voß, H. Bobadilla and V. Schenk for help during sampling. We are grateful to D. Garbe-Schönberg and U. Westernströer for help with ICP-MS analyses, to P. Appel and B. Mader for assistance with the electron microprobe and to A. Weinkauf for XRF analyses. Moreover, we wish to thank Marco Scambelluri for editorial handling of the manuscript and Ioannis Baziotis and Michael Bröcker for their detailed and constructive reviews that served to greatly improve the manuscript. Funding of this work by the Deutsche Forschungsgemeinschaft (SFB 574 "Volatiles and Fluids in Subduction Zones" at Kiel University and grant KO-3750/2 to MKS) is gratefully acknowledged. This is contribution no. 274 of the SFB 574.

References

Aguirre, L., Hervé, F., Godoy, E., 1972. Distribution of metamorphic facies in Chile: an outline. Krystallinikum 9, 7-19.

Arai, S., Matsukage, K., Isobe, E., Vysotskiy, S., 1997. Concentration of incompatible elements in oceanic mantle: Effect of melt/wall interaction in stagnant of failed melt conduits within peridotite. Geochimica et Cosmochimica Acta 61, 671-675.

Arghe, F., Skelton, A., Pitcairn, I., 2011. Spatial coupling between spilitization and carbonation of basaltic sills in SW Scottish Highlands: evidence of a mineralogical control of metamorphic fluid flow. Geofluids 11, 245-259.

Barrientos, X., Selverstone, J., 1993. Infiltration vs. thermal overprinting of epidote blueschist, Ile de Groix, France. Geology 21, 69-72.

Baziotis, I., Mposkos, E., 2011. Origin of metabasites from upper tectonic unit of the Lavrion area (SE Attica, Greece): Geochemical implications for dual origin with distinct provenance of blueschist and greenschist's protoliths. Lithos 126, 161-173.

Baziotis, I., Proyer, A., Mposkos, E., 2009. High-pressure/low-temperature metamorphism of basalts in Lavrion (Greece): implications for the preservation of peak metamorphic assemblages in blueschists and greenschists. European Journal of Mineralogy 21, 133-148.

Bebout, G.E., 2007. Metamorphic chemical geodynamics of subduction zones. Earth and Planetary Science Letters 260, 373-393.

Bebout, G.E., 2014. Chemical and isotopic cycling in subduction zones. In: Rudnick, R.L. (Ed.), The Crust. Treatise in Geochemistry 2nd Edition, vol. 4, pp. 703-747.

Bebout, G.E., Barton, M.D., 1993. Metasomatism during subduction: products and possible paths in the Catalina Schist, California. Chemical Geology 108, 61-92.

710 Bebout, G.E., Bebout, A.E., Graham, C.M., 2007. Cycling of B, Li, and LILE (K, Cs, Rb, Ba,
711 Sr) into subduction zones: SIMS evidence from micas in high-P/T metasedimentary
712 rocks. Chemical Geology 239, 284-304.
713 Becker, H., Jochum, K.P., Carlson, R.W., 2000. Trace element fractionation during
714 dehydration of eclogites from high-pressure terranes and the implications for element
715 fluxes in subduction zones. Chemical Geology 163, 65-99.
716 Beinlich, A., Klemd, R., John, T., Gao, J., 2010. Trace-element mobilization during Ca-
717 metasomatism along a major fluid conduit: Eclogitization of a blueschist as a
718 consequence of fluid-rock interaction. Geochimica et Cosmochimica Acta 74, 1892-
719 1922.
720 Beitter, T., Wagner, T., Markl, G., 2008. Formation of kyanite-quartz veins of the Alpe
721 Sponda, Central Alps, Switzerland: implications for Al transport during regional
722 metamorphism. Contributions to Mineralogy and Petrology 156, 689-707.
723 Bousquet, R., 2008. Metamorphic heterogeneities within a single HP unit: Overprint effect or
724 metamorphic mix? Lithos 103, 46-69.
725 Boynton, W.V., 1984. Geochemistry of the rare earth elements: meteorite studies. In:
726 Henderson, P. (Ed.), Rare Earth Element Geochemistry. Elsevier, Amsterdam, pp. 63-
727 114.
728 Breeding, C.M., Ague, J.J., Bröcker, M., 2004. Fluid-metasedimentary rock interactions in
729 subduction-zone mélange: Implications for the chemical composition of arc magmas.
730 Geology 32, 1041-1044.
731 Bröcker, M., 1990. Blueschist-to-greenschist transition in metabasites from Tinos Island,
732 Cyclades, Greece: Compositional control or fluid infiltration? Lithos 25, 25-29.
733 Bucholz, C.E., Ague, J.J., 2010. Fluid flow and Al transport during quartz-kyanite vein
734 formation, Unst, Shetland Islands, Scotland. Journal of Metamorphic Geology 28, 19-
735 39.

736 Clarke, G.L., Powell, R., Fitzherbert, J.A., 2006. The lawsonite paradox: a comparison of
737 field evidence and mineral equilibria modelling. Journal of Metamorphic Geology 24,
738 715-725.
739 Connolly, J.A.D., 1990. Multivariable phase diagrams: an algorithm based on generalized
740 thermodynamics. American Journal of Science 290, 666-718.
741 Connolly, J.A.D., 2005. Computation of phase equilibria by linear programming: A tool for
742 geodynamic modeling and its application to subduction zone decarbonation. Earth and
743 Planetary Science Letters 236, 524-541.
744 Diener, J.F.A., Powell, R., 2010. Influence of ferric iron on the stability of mineral
745 assemblages. Journal of Metamorphic Geology 28, 599-613.
746 Diener, J.F.A., Powell, R., White, R.W., Holland, T.J.B., 2007. A new thermodynamic model
747 for clino- and orthoamphiboles in the system Na_2O-CaO-FeO-MgO-Al_2O_3-SiO_2-H_2O-
748 O. Journal of Metamorphic Geology 25, 631-656.
749 Dungan, M.A., Vance, J.A., Blanchard, D.P., 1983. Geochemistry of the Shuksan greenschists
750 and blueschists, North Cascades, Washington: Variably fractionated and altered
751 metabasalts of oceanic affinity. Contributions to Mineralogy and Petrology 82, 131-146.
752 El Korh, A., Schmidt S.T., Ulianov, A., Potel, S. (2009). Trace element partitioning in HP–LT
753 metamorphic assemblages during subduction-related metamorphism, Ile de Groix,
754 France: a detailed LA-ICP-MS study. Journal of Petrology 50, 1107–1148.
755 El Korh, A., Schmidt, S.T., Vennemann, T., Ballèvre, M. (2013). Trace element and isotopic
756 fingerprints in HP-LT metamorphic rocks as a result of fluid-rock interactions (Ile de
757 Groix, France). Gondwana Research 23, 880-900.
758 El-Shazly, A.K., Worthing, M.A., Liou, J.G., 1997. Interlayered eclogites, blueschists and
759 epidote amphibolites from NE Oman: a record of protolith compositional control and
760 limited fluid infiltration. Journal of Petrology 38, 1461-1487.

761 Ernst, W.G., 1975. Systematics of large-scale tectonics and age progressions in Alpine and
762 Circum-Pacific blueschist belts. Tectonophysics 26, 229-246.
763 Ernst, W.G., 1988. Tectonic history of subduction zones inferred from retrograde blueschist
764 *P-T* paths. Geology 16, 1081-1084.
765 Ernst, W.G., 2006. Preservation/exhumation of ultrahigh-pressure subduction complexes.
766 Lithos 92, 321-335.
767 Evans, B.W., 1990. Phase relations of epidote-blueschists. Lithos 25, 3-23.
768 Evans, K.A., Powell, R., Frost, B.R., 2013. Using equilibrium thermodynamics in the study of
769 metasomatic alteration, illustrated by an application to serpentinites. Lithos 168-169,
770 67-84.
771 Fuhrmann, M.L., Lindsley, D.H., 1988. Ternary-feldspar modeling and thermometry.
772 American Mineralogist 73, 201-215.
773 Garbe-Schönberg, C.D., 1993. Simultaneous determination of 37 trace elements in 28
774 international rock standards by ICP-MS. Geostandard Newsletter 17, 81-97.
775 Glodny, J., Bingen, B., Austrheim, H., Molina, J.F., Rusin, A., 2002. Precise eclogitization
776 ages deduced from Rb/Sr mineral systematics: The Maksyutov complex, Southern
777 Urals, Russia. Geochimica et Cosmochimica Acta 66, 1221-1235.
778 Glodny, J., Kühn, A., Austrheim, H., 2008. Diffusion versus recrystallization processes in Rb-
779 Sr geochronology: Isotopic relics in eclogite facies rocks, Western Gneiss Region,
780 Norway. Geochimica et Cosmochimica Acta 72, 506-525.
781 Goncalves, P., Oliot, E., Marquer, D., Connolly, J.A.D., 2012. Role of chemical processes on
782 shear zone formation: an example from the Grimsel metagranodiorite (Aar massif,
783 Central Alps). Journal of Metamorphic Geology 30, 703-722.
784 Goncalves, P., Marquer, D., Oliot, E., Durand, C., 2013. Thermodynamic modeling and
785 thermobarometry of metasomatized rocks. In: Harlov, D., Austhreim, H. (Eds.),

786 Metasomatism and the chemical transformation of rock. Lecture Notes in Earth System
787 Sciences, Springer-Verlag Berlin Heidelberg, pp. 53-91.
788 González-Bonorino, F., 1971. Metamorphism of the crystalline basement of Central Chile.
789 Journal of Petrology 12, 149-175.
790 Grant, J.A., 1986. The Isocon diagram - a simple solution to Gresens' equation for
791 metasomatic alteration. Economic Geology 81, 1976-1982.
792 Grant, J.A., 2005. Isocon analysis: A brief review of the method and applications. Physics and
793 Chemistry of the Earth 30, 997-1004.
794 Guiraud, M., Powell, R., Rebay, G, 2001. H_2O in metamorphism and unexpected behaviour in
795 the preservation of metamorphic mineral assemblages. Journal of Metamorphic
796 Geology 19, 445-454.
797 Halama, R., John, T., Herms, P., Hauff, F., Schenk, V., 2011. A stable (Li, O) and radiogenic
798 (Sr, Nd) isotope perspective on metasomatic processes in a subducting slab. Chemical
799 Geology 281, 151-166.
800 Halama, R., Konrad-Schmolke, M., Sudo, M., Marschall, H.R., Wiedenbeck, M., 2014.
801 Effects of fluid-rock interaction on $^{40}Ar/^{39}Ar$ geochronology in high-pressure rocks
802 (Sesia-Lanzo Zone, Western Alps). Geochimica et Cosmochimica Acta 126, 475-494.
803 Halama, R., Savov, I.P., Garbe-Schönberg, D., Schenk, V., Toulkeridis, T., 2013. Vesuvianite
804 in high-pressure-metamorphosed oceanic lithosphere (Raspas Complex, Ecuador) and
805 its role for transport of water and trace elements in subduction zones. European Journal
806 of Mineralogy 25, 193-219.
807 Heinrich, C.A., 1982. Kyanite-eclogite to amphibolite facies evolution of hydrous mafic to
808 pelitic rocks, Adula Nappe, Central Alps. Contributions to Mineralogy and Petrology
809 81, 30-38.
810 Hervé, F., 1988. Late Paleozoic subduction and accretion in southern Chile. Episodes 11, 183-
811 188.

812 Hervé, F., Faundez, V., Calderón, M., Massonne, H.-J., Willner, A.P., 2007. Metamorphic
813 and plutonic basement complexes. In: Moreno, T., Gibbons, W. (Eds.), The Geology of
814 Chile. The Geological Society, London, pp. 5-19.
815 Hervé, F., Munizaga, F., Godoy, E., Aguirre, L., 1974. Late Paleozoic K/Ar ages of
816 blueschists from Pichilemu, Central Chile. Earth and Planetary Science Letters 23, 261-
817 264.
818 Hervé, F., Munizaga, F., Parada, M.A., Brook, M., Pankhurst, R.J., Snelling, N.J., Drake, R.,
819 1988. Granitoids of the coast range of central Chile: Geochronology and geologic
820 setting. Journal of South American Earth Sciences 1, 185-194.
821 Holland, T., Baker, J., Powell, R., 1998. Mixing properties and activity-composition
822 relationships of chlorites in the system MgO-FeO-Al_2O_3-SiO_2-H_2O. European Journal
823 of Mineralogy 10, 395-406.
824 Holland, T., Powell, R., 1998. An internally consistent thermodynamic data set for phases of
825 petrological interest. Journal of Metamorphic geology 16, 309-343.
826 Hyppolito, T., Juliani, C., García-Casco, A., Meira, V.T., Bustamante, A., Hervé, F. (2014).
827 The nature of the Palaeozoic oceanic basin at the southwestern margin of Gondwana
828 and implications for the origin of the Chilenia terrane (Pichilemu region, central Chile).
829 International Geology Review 56, 1097-1121.
830 Jacques, G., Hoernle, K., Gill, J., Hauff, F., Wehrmann, H., Garbe-Schönberg, D., van den
831 Bogaard, P., Bindeman, I., Lara, L.E., 2013. Across-arc geochemical variations in the
832 Southern Volcanic Zone, Chile (34.5-38.0°S): Constraints on mantle wedge and slab
833 input compositions. Geochimica et Cosmochimica Acta 123, 218-243.
834 John, T., Klemd, R., Gao, J., Garbe-Schönberg, C.D., 2008. Trace-element mobilization in
835 slabs due to non steady-state fluid-rock interaction: constraints from an eclogite-facies
836 transport vein in blueschist (Tianshan, China). Lithos 103, 1-24.

837 John, T., Scherer, E., Haase, K.M., Schenk, V., 2004. Trace element fractionation during
838 fluid-induced eclogitization in a subducting slab: trace element and Lu-Hf/Sm-Nd
839 isotope systematics. Earth and Planetary Science Letters 227, 441-456.
840 John, T., Scherer, E., Schenk, V., Herms, P., Halama, R., Garbe-Schönberg, D., 2010.
841 Subducted seamounts in an eclogite-facies ophiolite sequence: The Andean Raspas
842 Complex, SW Ecuador. Contributions to Mineralogy and Petrology 159, 265-284.
843 Kahl, W.-A., Schumacher, J.C., 2000. Multiple pyroxene and amphibole assemblages in the
844 amphibolite facies: Bulk compositional controls. American Mineralogist 85, 1606-1616.
845 Konrad-Schmolke, M., O'Brien, P.J., de Capitani, C., Carswell, D.A., 2008. Garnet growth at
846 high- and ultra-high pressure conditions and the effect of element fractionation on
847 mineral modes and composition. Lithos 103, 309-332.
848 Konrad-Schmolke, M., O'Brien, P.J., Zack, T., 2011. Fluid migration above a subducted slab
849 – constraints on amount, pathways and major element mobility from partially
850 overprinted eclogite-facies rocks (Sesia Zone, Western Alps). Journal of Petrology 52,
851 457-486.
852 Leake, B.E. et al., 1997. Nomenclature of amphiboles: report of the subcommittee on
853 amphiboles of the International Mineralogical Association, Commission on New
854 Minerals and Mineral Names. Canadian Mineralogist 35, 219-246.
855 Li, X.-P., Rahn, M., Bucher, K., 2004. Metamorphic processes in rodingites of the Zermatt-
856 Saas ophiolites. International Geology Reviews 46, 28-51.
857 Locock, A.J., 2014. An Excel spreadsheet to classify chemical analyses of amphiboles
858 following the IMA 2012 recommendations. Computers & Geosciences 62, 1-11.
859 López-Carmona, A., Pitra, P., Abati, J., 2013. Blueschist-facies metapelites from the Malpica-
860 Tui Unit (NW Iberian Massif): phase equilibria modelling and H_2O and Fe_2O_3 influence
861 in high-pressure assemblages. Journal of Metamorphic Geology 31, 263-280.

Lucassen, F., Trumbull, R., Franz, G., Creixell, C., Vásquez, P., Romer, R.L., Figueroa, O., 2004. Distinguishing crustal recycling and juvenile additions at active continental margins: the Paleozoic to recent compositional evolution of the Chilean continental margin (36-41°S). Journal of South American Earth Sciences 17, 103-119.

Lucassen, F., Wiedicke, M., Franz, G., 2010. Complete recycling of a magmatic arc: evidence from chemical and isotopic composition of Quaternary trench sediments in Chile (36°-40°S). International Journal of Earth Sciences 99, 687-701.

Marschall, H.R., Altherr, R., Gméling, K., Kasztovszky, Z., 2009. Lithium, boron and chlorine as tracers for metasomatism in high-pressure metamorphic rocks: a case study from Syros (Greece). Mineralogy and Petrology 95, 291-302.

Maruyama, S., Cho, M., Liou, J.G., 1986. Experimental investigations of blueschist-greenschist transition equilibria: pressure dependence of Al_2O_3 contents in sodic amphiboles – a new geobarometer. In: Evans, B.E., Brown, E.H. (Eds.), Blueschists and Eclogites. Geological Society of America Memoir, vol. 164, pp. 1-16.

Massonne, H.-J., Willner, A.P., 2008. Phase relations and dehydration behaviour of psammopelite and mid-ocean ridge basalt at very-low-grade to low-grade metamorphic conditions. European Journal of Mineralogy 20, 867-879.

Miller, D.P., Marschall, H.R., Schumacher, J.C., 2009. Metasomatic formation and petrology of blueschist-facies hybrid rocks from Syros (Greece): Implications for reactions at the slab-mantle interface. Lithos 107, 53-67.

Munizaga, F., Aguirre, L., Hervé, F., 1973. Rb/Sr ages of rocks from the Chilean metamorphic basement. Earth and Planetary Science Letters 18, 87-92.

Oberhänsli, R., 1978. Chemische Untersuchungen an Glaukophan-führenden basischen Gesteinen aus den Bündnerschiefern Graubündens. Schweizerische Mineralogische und Petrographische Mitteilungen 58, 139-156.

887 Oh, C.W., Liou, J.G., Maruyama, S., 1991. Low-temperature eclogites and eclogitic schists in
888 Mn-rich metabasites in Ward Creek, California; Mn and Fe effects on the transition
889 between blueschist and eclogite. Journal of Petrology 32, 275-301.
890 Okrusch, M., Bröcker, M., 1990. Eclogites associated with high-grade blueschists in the
891 Cyclades archipelago, Greece; a review. European Journal of Mineralogy 2, 451-478.
892 Pattison, D., 2013. Regional metamorphism in the Ballachulish area, SW Highlands,
893 Scotland: new perspectives on a famous old debate, with regional implications. Journal
894 of the Geological Society of London 170, 417-434.
895 Pearce, J.A., 2008. Geochemical fingerprinting of oceanic basalts with applications to
896 ophiolite classification and the search for Archean oceanic crust. Lithos 100, 14-48.
897 Pearce, J.A., Cann, J.R., 1973. Tectonic setting of basic volcanic rocks determined using trace
898 element analyses. Earth and Planetary Science Letters 19, 290-300.
899 Penniston-Dorland, S.C., Sorensen, S.S., Ash, R.D., Khadke, S.V., 2010. Lithium isotopes as
900 a tracer of fluids in a subduction zone mélange: Franciscan Complex, CA. Earth and
901 Planetary Science Letters 292, 181-190.
902 Philippot, P., Selverstone, J., 1991. Trace-element-rich brines in eclogitic veins: implications
903 for fluid composition and transport during subduction. Contributions to Mineralogy and
904 Petrology 106, 417-430.
905 Platt, J.P., 1993. Exhumation of high-pressure rocks: a review of concepts and processes.
906 Terra Nova 5, 119-133.
907 Pognante, U., Kienast, J.-R., 1987. Blueschist and eclogite transformations in Fe-Ti gabbros:
908 A case from the Western Alps ophiolites. Journal of Petrology 28, 271-292.
909 Putlitz, B., Matthews, A., Valley, J.W., 2000. Oxygen and hydrogen isotope study of high-
910 pressure metagabbros and metabasalts (Cyclades, Greece): implications for the
911 subduction of oceanic crust. Contributions to Mineralogy and Petrology 138, 114-126.

912 Richter, P.P., Ring, U., Willner, A.P., Leiss, B., 2007. Structural contacts in subduction
913 complexes and their tectonic significance: The Late Paleozoic coastal accretionary
914 wedge of central Chile. Journal of the Geological Society of London 164, 203-214.
915 Ridley, J., 1984. Evidence of a temperature-dependent 'blueschist' to 'eclogite' transformation
916 in high-pressure metamorphism of metabasic rocks. Journal of Petrology 25, 852-870.
917 Schliestedt, M., Matthews, A., 1987. Transformation of blueschist to greenschist facies rocks
918 as a consequence of fluid infiltration, Sifnos (Cyclades), Greece. Contributions to
919 Mineralogy and Petrology 97, 237-250.
920 Scott, J.M., Konrad-Schmolke, M., O'Brien, P.J., Günter, C., 2013. High-T, low-P formation
921 of rare olivine-bearing symplectites in Variscan eclogite. Journal of Petrology 54, 1375-
922 1398.
923 Selverstone, J., Franz, G., Thomas, S., Getty, S., 1992. Fluid variability in 2 GPa eclogites as
924 an indicator of fluid behavior during subduction. Contributions to Mineralogy and
925 Petrology 112, 341-357.
926 Sorensen, S.S., Grossman, J.N., Perfit, M.R., 1997. Phengite-hosted LILE-enrichment in
927 eclogite and related rocks: implications for fluid-mediated mass-transfer in subduction
928 zones and arc magma genesis. Journal of Petrology 38, 3-34.
929 Spandler, C., Hermann, J., Arculus, R., Mavrogenes, J., 2004. Geochemical heterogeneity and
930 element mobility in deeply subducted oceanic crust; insights from high-pressure mafic
931 rocks from New Caledonia. Chemical Geology 206, 21-42.
932 Staudigel, H., 2003. Hydrothermal alteration processes in the oceanic crust. In: Rudnick, R.L.
933 (Ed.), The Crust. Treatise on Geochemistry, vol. 3, pp. 511-535.
934 Staudigel, H., Hart, S.R., 1983. Alteration of basaltic glass: Mechanisms and significance of
935 the oceanic crust-seawater budget. Geochimica et Cosmochimica Acta 47, 337-350.
936 Sun, S.-S., McDonough, W.F., 1989. Chemical and isotopic systematics of oceanic basalts:
937 implications for mantle composition and processes. In: Saunders, A.D., Norry, M.J.

(Eds.), Magmatism in the ocean basins. Geological Society of London, Special Publication 42, 313-345.

Vallis, F., Scambelluri, M., 1996. Redistribution of high-pressure fluids during retrograde metamorphism of eclogite-facies rocks (Voltri Massif, Italian Western Alps). Lithos 39, 81-92.

van der Straaten, F., Halama, R., John, T., Schenk, V., Hauff, F., Andersen, N., 2012. Tracing the effects of high-pressure metasomatic fluids and seawater alteration in blueschist-facies overprinted eclogites: Implications for subduction channel processes. Chemical Geology 292-293, 69-87.

van der Straaten, F., Schenk, V., John, T., Gao, J., 2008. Blueschist-facies rehydration of eclogites (Tian Shan, NW-China): implications for fluid-rock interaction in the subduction channel. Chemical Geology 225, 195-219.

Verlaguet, A., Goffé, B., Brunet, F., Poinssot, C., Vidal, O., Findling, N., Menut, D., 2011. Metamorphic veining and mass transfer in a chemically closed system: a case study in Alpine metabauxites (western Vanoise). Journal of Metamorphic Geology 29, 275-300.

Walther, J.V., Orville, P.M., 1982. Volatile production and transport in regional metamorphism. Contributions to Mineralogy and Petrology 79, 252-257.

Wangen, M., Munz, I.A., 2004. Formation of quartz veins by local dissolution and transport of silica. Chemical Geology 209, 179-192.

Widmer, T., Thompson, A.B., 2001. Local origin of high pressure vein material in eclogite facies rocks of the Zermatt-Saas Zone, Switzerland. American Journal of Science 301, 627-656.

Willner, A.P., 2005. Pressure-Temperature evolution of a late Palaeozoic paired metamorphic belt in North-Central Chile (34°-35°30'S). Journal of Petrology 46, 1805-1833.

963 Willner, A.P., Hervé, F., Massonne, H.-J., 2000. Mineral chemistry and pressure-temperature
964 evolution of two contrasting high-pressure - low-temperature belts in the Chonos
965 Archipelago, Southern Chile. Journal of Petrology 41, 309-330.
966 Willner, A.P., Richter, P.P., Ring, U., 2009. Structural overprint of a late Paleozoic
967 accretionary system in north-central Chile (34°-35°S) during post-accretional
968 deformation. Andean Geology 36, 17-36.
969 Willner, A.P., Thomson, S.N., Kröner, A., Wartho, J.-A., Wijbrans, J.R., Hervé, F., 2005.
970 Time markers for the evolution and exhumation history of a late Palaeozoic paired
971 metamorphic belt in North-Central Chile. Journal of Petrology 46, 1835-1858.
972
973

Figure captions:

Fig. 1: Geological map of the Western and Eastern Series between 34° and 35°40’ S with the sample location at Pichilemu (modified from Willner et al., 2005; 2009).

Fig. 2: Photographs of layered blueschist-greenschist outcrops at Infiernillo Beach in Pichilemu. Note the distinct color difference between the blueschist and the greenschist layers.

Fig. 3: Back-scattered electron images of blueschist and greenschist layers. A) Blueschist layer comprising glaucophane cores overgrown by sodic-calcic to calcic amphibole (winchite-actinolite), together with larger winchites and small actinolites. Winchite contains inclusions of titanite. Albite, chlorite and phengite are present in the matrix. B) Greenschist layer showing the typical fine-grained texture of both greenschist and blueschist layers. Compared to the blueschist layer, albite occurs less frequently and large patches of chlorite are conspicuous. C) Blueschist layer with a patchy occurrence of glaucophane and winchite and aggregates of titanite. D) Greenschist layer that contains a relatively large glaucophane overgrown by actinolite. E) Amphibole porphyroblast comprising a core of ferro-winchite surrounded by glaucophane. Note that the porphyroblast is not aligned with the foliation, in contrast to actinolite in the matrix. F) Greenschist layer with relict Ti-rich ferropargasite in actinolite. Similar relicts, interpreted to derive from the igneous protolith, occur in the corresponding blueschist sample. Mineral abbreviations: ab – albite, act – actinolite, ap – apatite, chl – chlorite, gln – glaucophane, phg – phengite, Ti-fpg – Ti-rich ferropargasite, ttn – titanite, win – winchite, zrn – zircon.

Fig. 4: Amphibole major element chemistry. A) Na_B versus Si_T. Note the large compositional variation from almost pure actinolite to almost pure glaucophane. B) Mg#, defined as $Mg/(Mg+Fe^{2+}+Fe^{3+})$, versus Ca_B. There is a general broad positive correlation, only the relict Ti-rich ferropargasites fall off the trend.

Fig. 5: Chondrite-normalized (Boynton, 1984) REE diagrams. Panels A)-C) show three blueschist-greenschist pairs with similar REE patterns. In contrast, panel D) shows large compositional differences between the three adjacent layers of sample CH-1-48 and the overall variability observed in the entire sequence. REE patterns of typical oceanic OIBs (alkalic OIB and N-MORB from Sun and McDonough (1989), tholeiitic OIB is the standard BHVO-1) and volcanic rocks from the Chilean volcanic front (Jacques et al., 2013) are shown for comparison.

Fig. 6: Layered blueschists and greenschists plotted in the Th/Yb vs. Nb/Yb diagram of Pearce (2008). All samples fall into the field of the oceanic basalts and are distinct from volcanic rocks of the Southern Volcanic Zone (Jacques et al., 2013) and Quaternary trench sediments from the Chilean coast (Lucassen et al., 2010). E-MORB and alkalic OIB compositions are from Sun and McDonough (1989), tholeiitic OIB is the standard BHVO-1.

Fig. 7: Evaluation of igneous differentiation trends. In most cases, blueschist-greenschist pairs show variations that are inconsistent with igneous differentiation alone as the compositions plot either off typical differentiation trends, or they show compositional changes that are oblique to the trends (see text for details). Typical ocean island igneous differentiation trends are shown as small grey dots, represented by 161 selected analyses from the island of Jan Mayen (North Atlantic) taken from the GEOROC database. Blue and green symbols represent blueschist and greenschists, respectively.

Fig. 8: Diagrams based on key trace element abundances and ratios to distinguish between seafloor alteration and subduction-related metasomatic alteration with trends from Bebout (2007). Data sources for MORB and OIB compositions as in Figs. 5 and 6.

Fig. 9: Isocon diagrams (after Grant, 2005) of three blueschist-greenschist pairs to illustrate the geochemical variability. The solid lines are the slopes based on the elements considered as immobile, dashed lines are the slopes for the four LILE K, Ba, Rb and Cs. The 1:1 line is shown for comparison.

Fig. 10: Thermodynamic calculations (see Methodology for details) for a representative blueschist-greenschist pair. A) and B) show pseudosections calculated for H_2O-saturated conditions buffered by the hematite-magnetite (HM) buffer. The molar percentage of water bound in solids is indicated by the contours and the corresponding black numbers. The white lines give the modal proportion of chlorite in vol%. The thick white arrow indicates the retrograde P-T path of Willner (2005). C) and D) show P-X_{H2O} diagrams with the appearance of major mineral phases indicated at the boundaries of the different phase assemblages and the modal abundance of chlorite shown by the grey contours. E) and F) show P-X_{H2O} diagrams with contours of modal amphibole abundance. To illustrate the compositional variation of amphibole, the glaucophane component is shown by the thin black lines. The glaucophane component was calculated as $Na_2O - 0.5 \times O_2$ based on the definition in the amphibole solution model. Mineral abbreviations: Ab – albite, Chl – chlorite, Phg – phengite, Ep – epidote, Law – lawsonite, Omph – omphacite, Amph – amphibole, Grt – garnet, Kfsp – alkali feldspar.

Fig. 11: P-X diagrams of a representative blueschist-greenschist pair using the blueschist (left) and greenschist (right) composition as end-members on the x-axis. The appearance of key mineral phases shows only small differences between the two compositions. A) Diagram contoured for the modal proportions of chlorite. B) Diagram contoured for the modal proportion of amphibole with the values for the glaucophane component shown by the white lines. Mineral abbreviations are as for Fig. 10.

Tables:

Table 1: Whole-rock geochemical analyses of blueschist and greenschist samples from Pichilemu and basaltic reference material BHVO-2.

Table 2: Modal mineral proportions of three selected blueschist-greenschist pairs.

Electronic Appendix:

Representative microprobe analyses of amphibole, white mica, chlorite and feldspar in blueschists and greenschists from Pichilemu.

Fig. 1

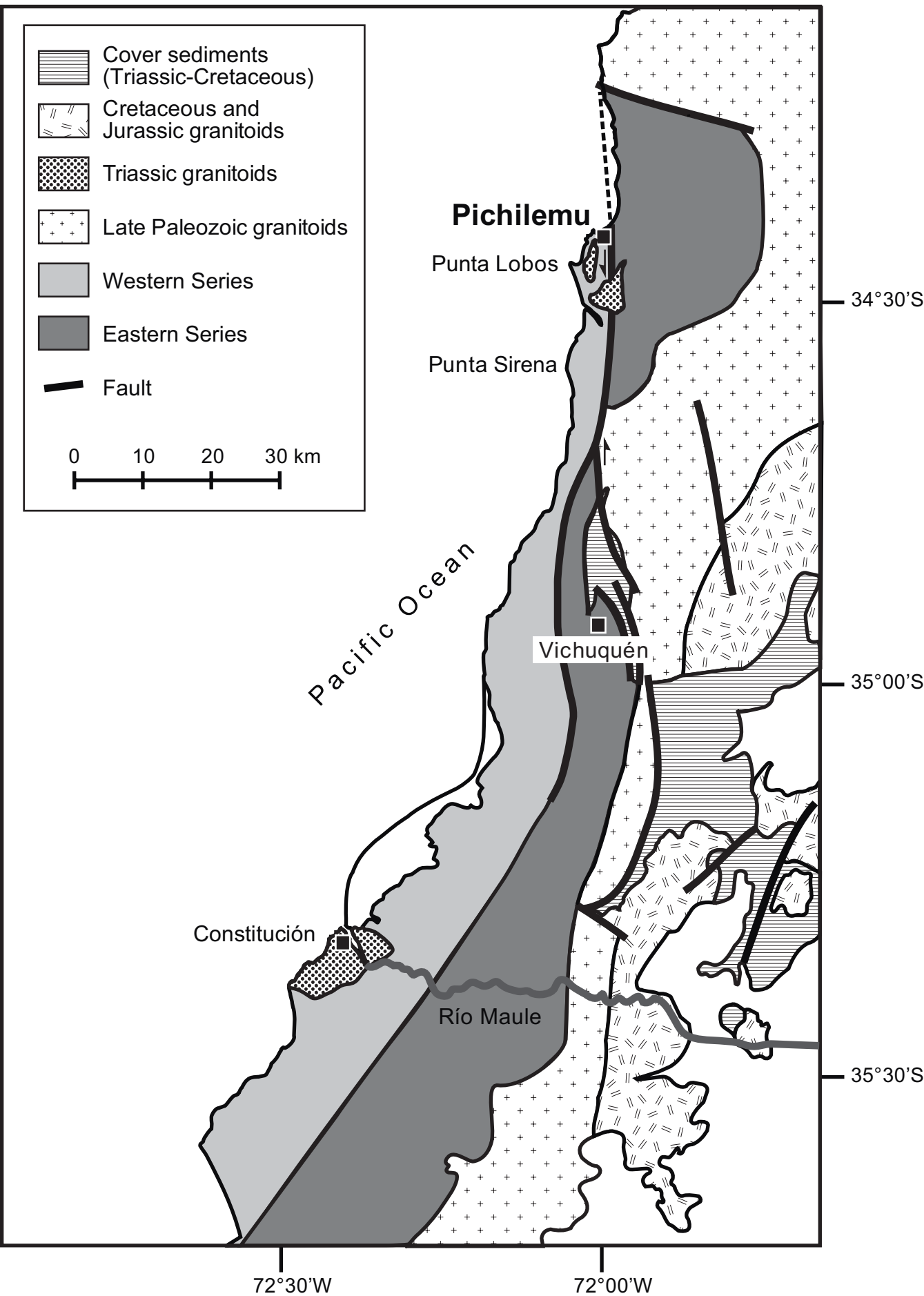
Cover sediments
(Triassic-Cretaceous)
Cretaceous and
Jurassic granitoids
Triassic granitoids
Late Paleozoic granitoids
Western Series
Eastern Series
Fault
0
10
20
30 km
Pichilemu
Punta Lobos
Punta Sirena
Pacific Ocean
Vichuquén
Constitución
Río Maule
34°30'S
35°00'S
35°30'S
72°30'W
72°00'W

Fig. 2

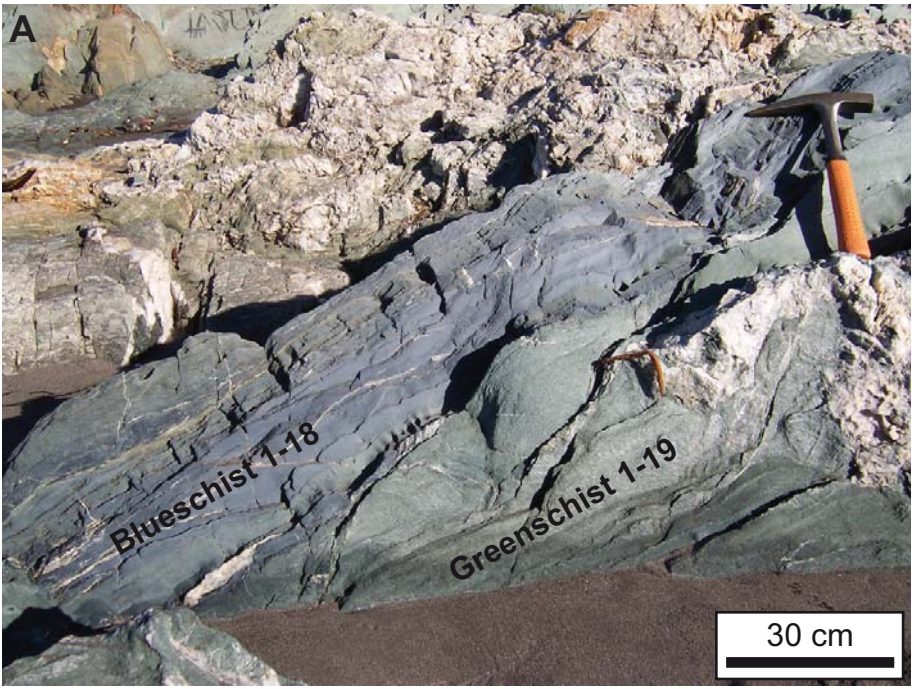
A
Blueschist 1-18
Greenschist 1-19
30 cm

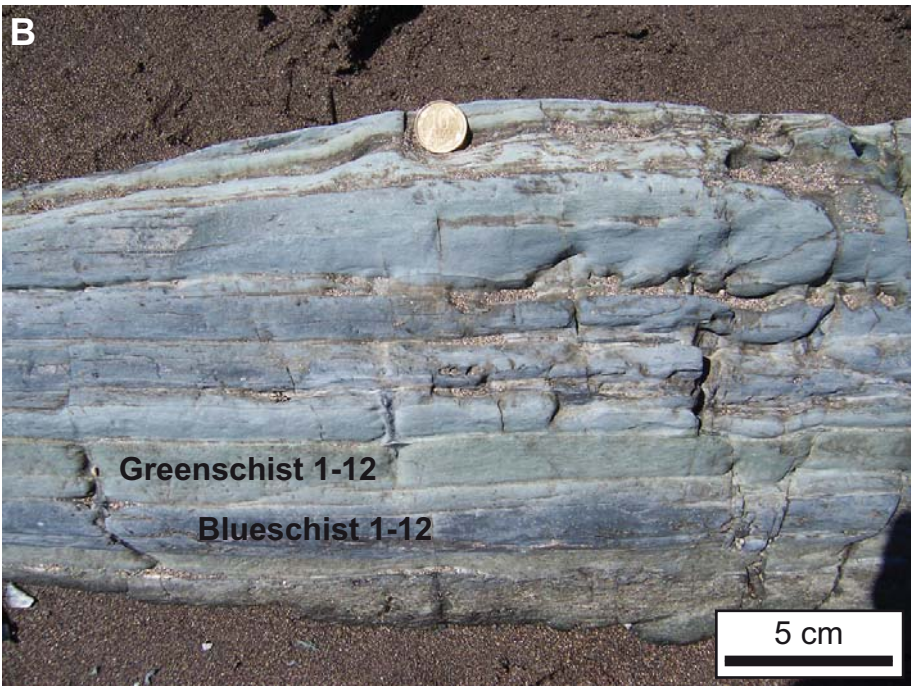
B
Greenschist 1-12
Blueschist 1-12
5 cm

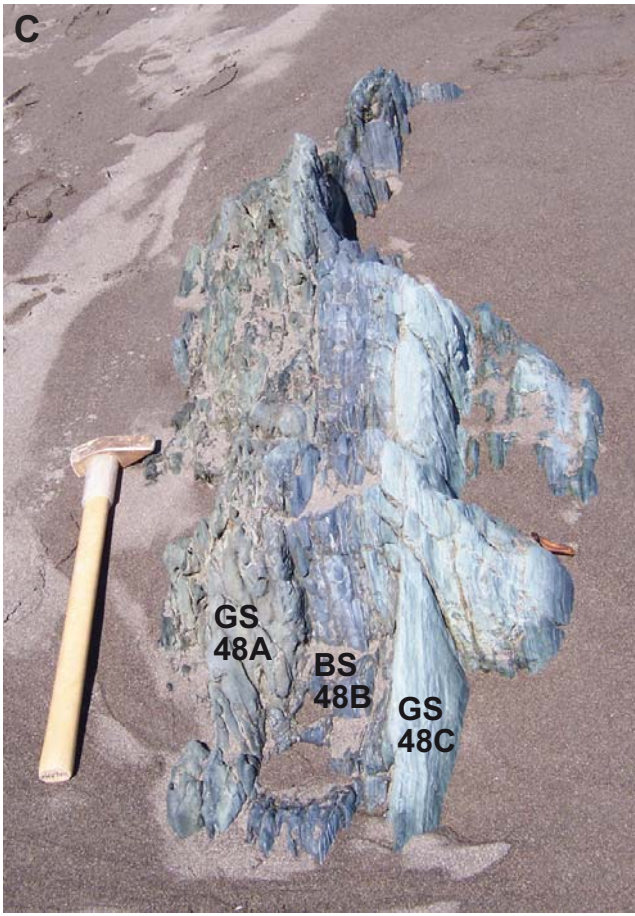
C
GS
48A
BS
48B
GS
48C

Fig. 3

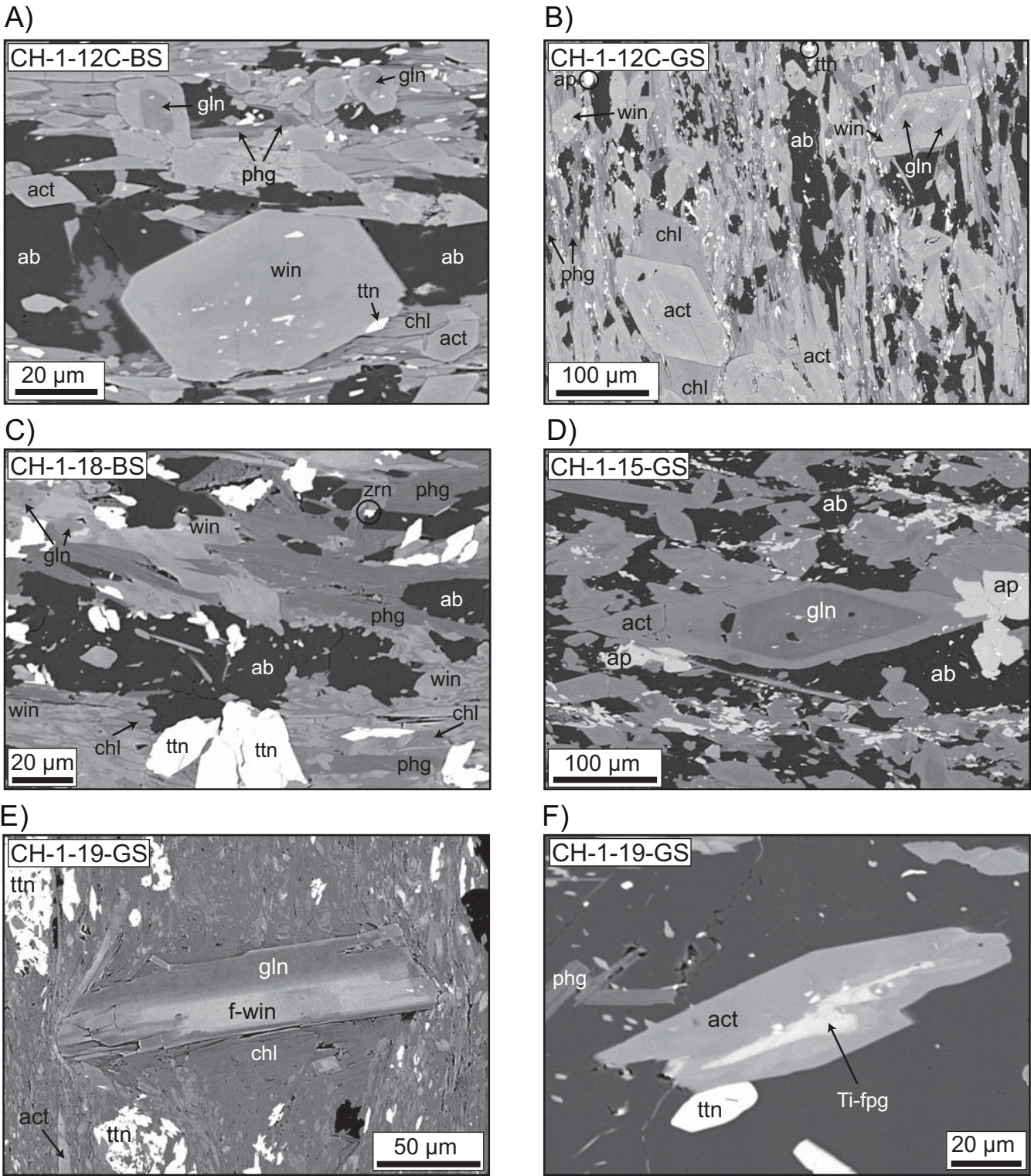
A)
CH-1-12C-BS
gln
gln
phg
act
ab
win
ab
ttn
chl
act
20 µm
B)
CH-1-12C-GS
ttn
ap
win
ab
win
gln
chl
phg
act
act
100 µm
chl
C)
CH-1-18-BS
zrn
phg
win
gln
ab
phg
ab
win
win
chl
chl
ttn
ttn
20 µm
phg
D)
CH-1-15-GS
ab
ap
gln
act
ap
ab
100 µm
E)
CH-1-19-GS
ttn
gln
f-win
chl
act
ttn
50 µm
F)
CH-1-19-GS
phg
act
Ti-fpg
ttn
20 µm

Fig. 4

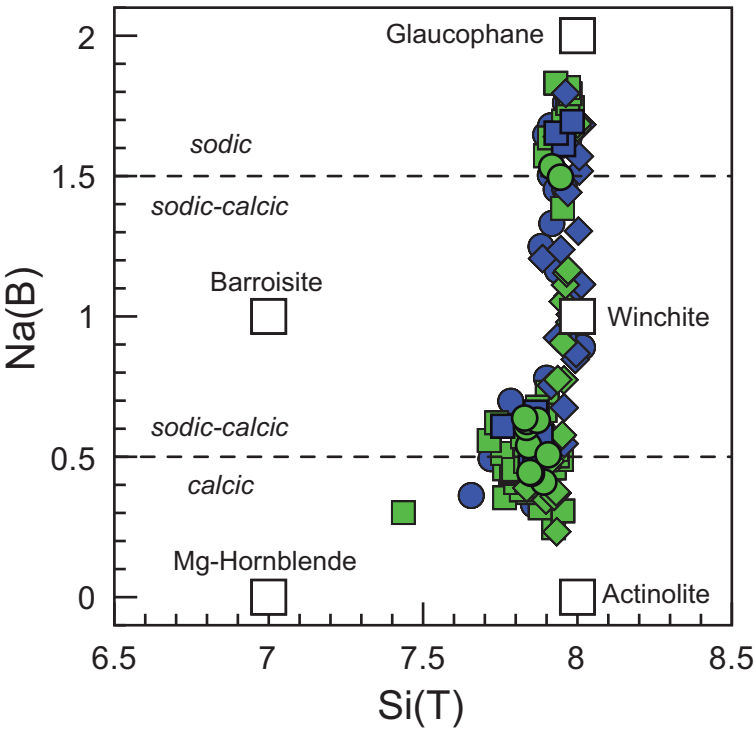
Glaucophane
sodic
sodic-calcic
Barroisite
Winchite
sodic-calcic
calcic
Mg-Hornblende
Actinolite
Na(B)
Si(T)
2
1.5
1
0.5
0
6.5
7
7.5
8
8.5

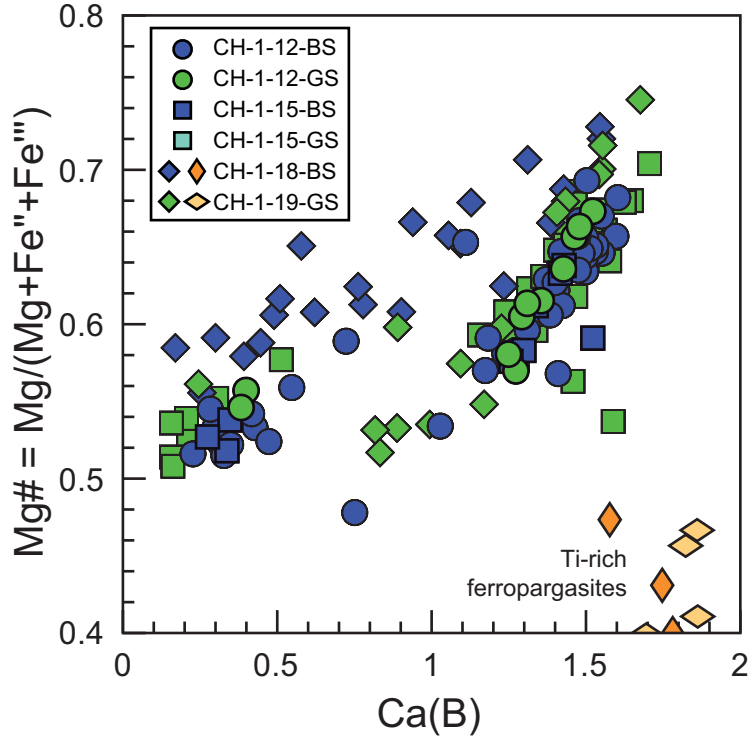
CH-1-12-BS
CH-1-12-GS
CH-1-15-BS
CH-1-15-GS
CH-1-18-BS
CH-1-19-GS
Ti-rich
ferropargasites
Mg# = Mg/(Mg+Fe"+Fe''')
Ca(B)
0.8
0.7
0.6
0.5
0.4
0
0.5
1
1.5
2

Fig. 5

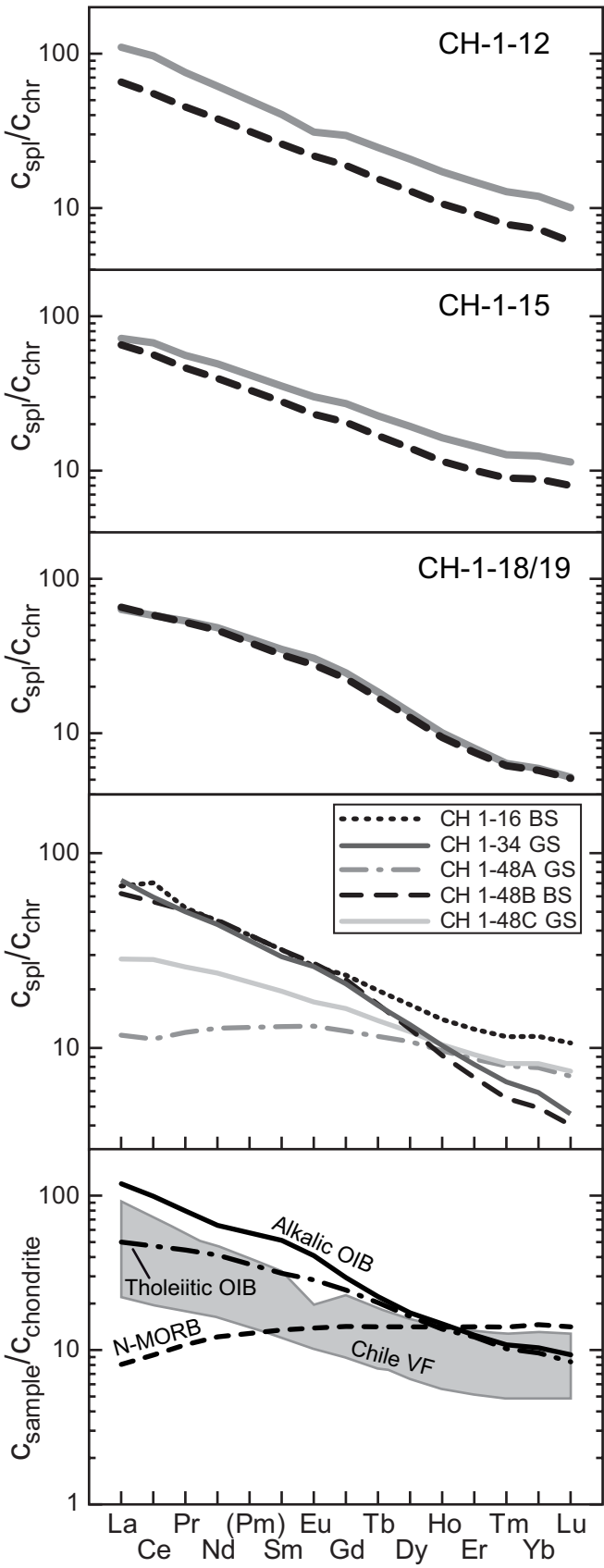
CH-1-12
CH-1-15
CH-1-18/19
CH 1-16 BS
CH 1-34 GS
CH 1-48A GS
CH 1-48B BS
CH 1-48C GS
Alkalic OIB
Tholeiitic OIB
N-MORB
Chile VF
100
10
1
La
Ce
Pr
Nd
(Pm)
Sm
Eu
Gd
Tb
Dy
Ho
Er
Tm
Yb
Lu

Fig. 6

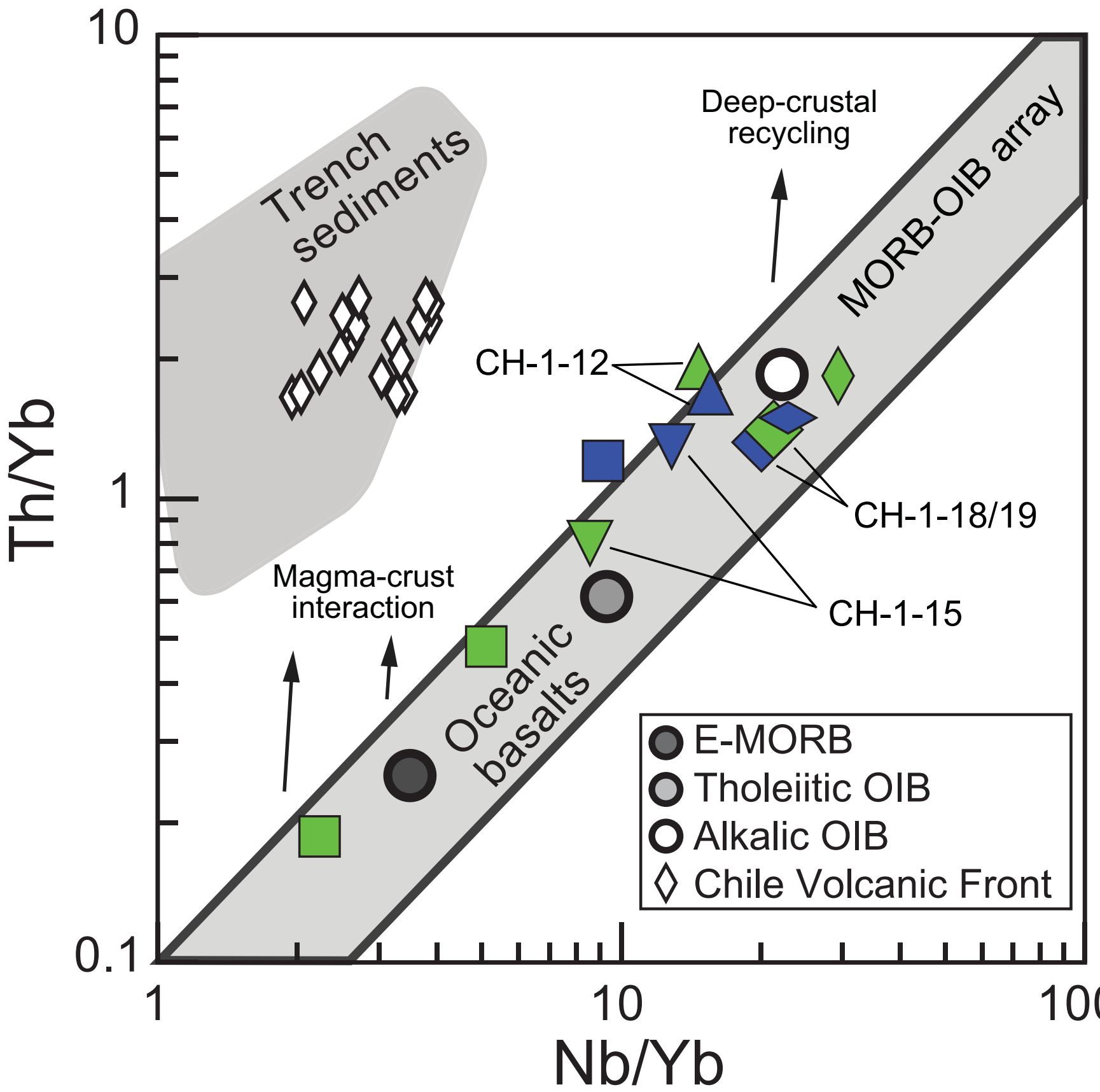
10
1
0.1
Th/Yb
1
10
100
Nb/Yb
Trench sediments
Deep-crustal recycling
MORB-OIB array
CH-1-12
CH-1-18/19
CH-1-15
Magma-crust interaction
Oceanic basalts
E-MORB
Tholeiitic OIB
Alkalic OIB
Chile Volcanic Front

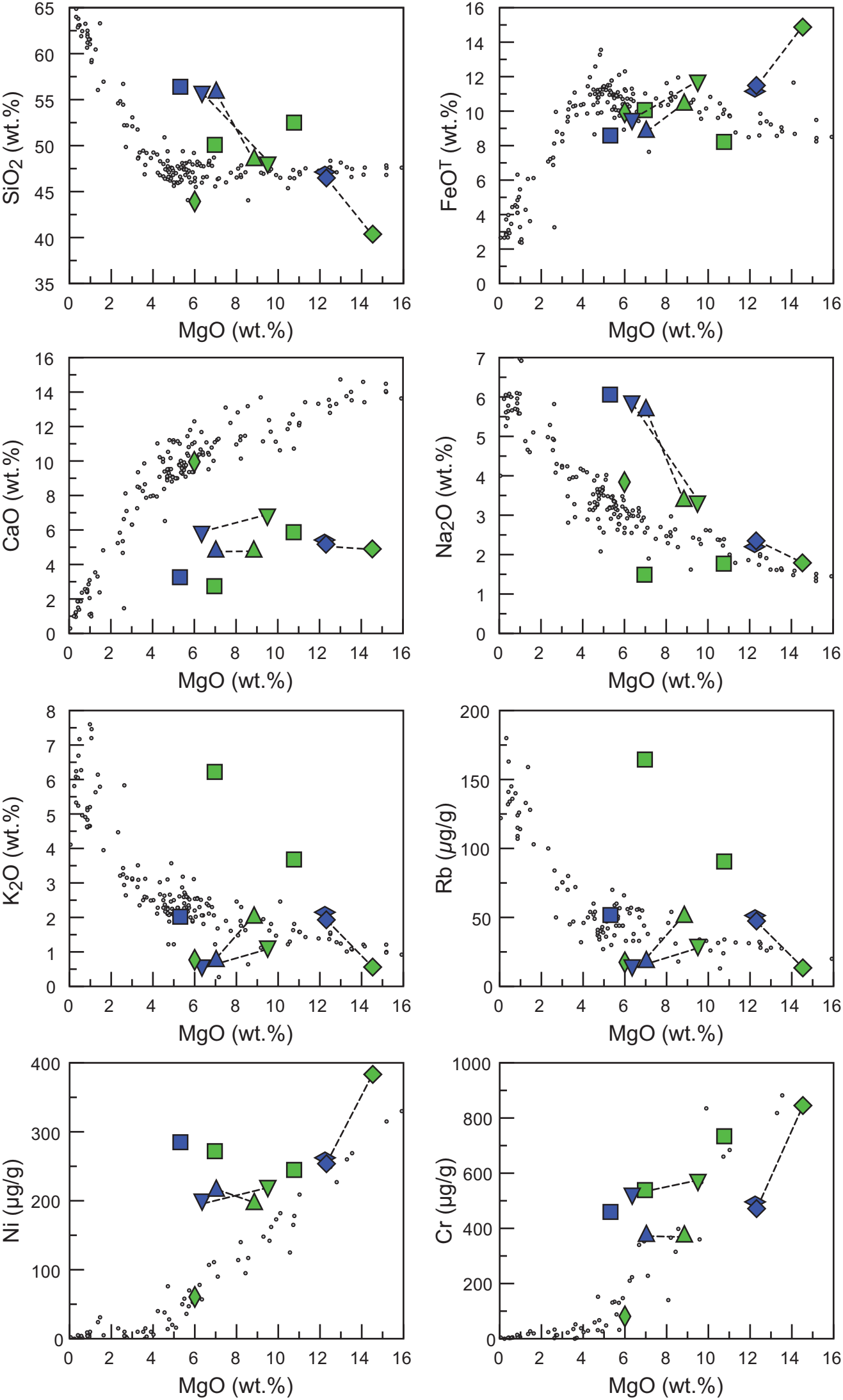
SiO2 (wt.%)
MgO (wt.%)
FeOT (wt.%)
MgO (wt.%)
CaO (wt.%)
MgO (wt.%)
Na2O (wt.%)
MgO (wt.%)
K2O (wt.%)
MgO (wt.%)
Rb (μg/g)
MgO (wt.%)
Ni (μg/g)
MgO (wt.%)
Cr (μg/g)
MgO (wt.%)

Fig. 7

Fig. 8

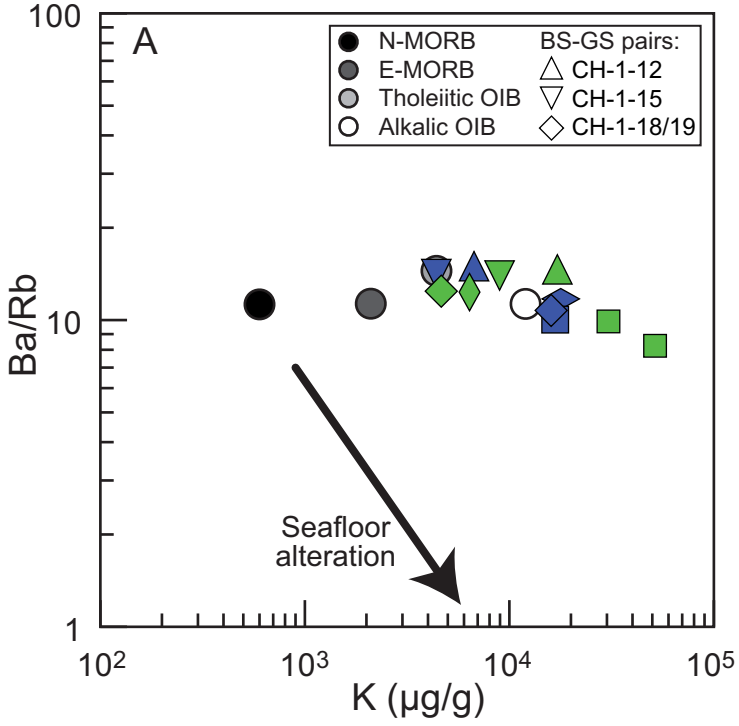
A
N-MORB
E-MORB
Tholeiitic OIB
Alkalic OIB
BS-GS pairs:
CH-1-12
CH-1-15
CH-1-18/19
Ba/Rb
100
10
1
Seafloor
alteration
10^2
10^3
10^4
10^5
K (μg/g)

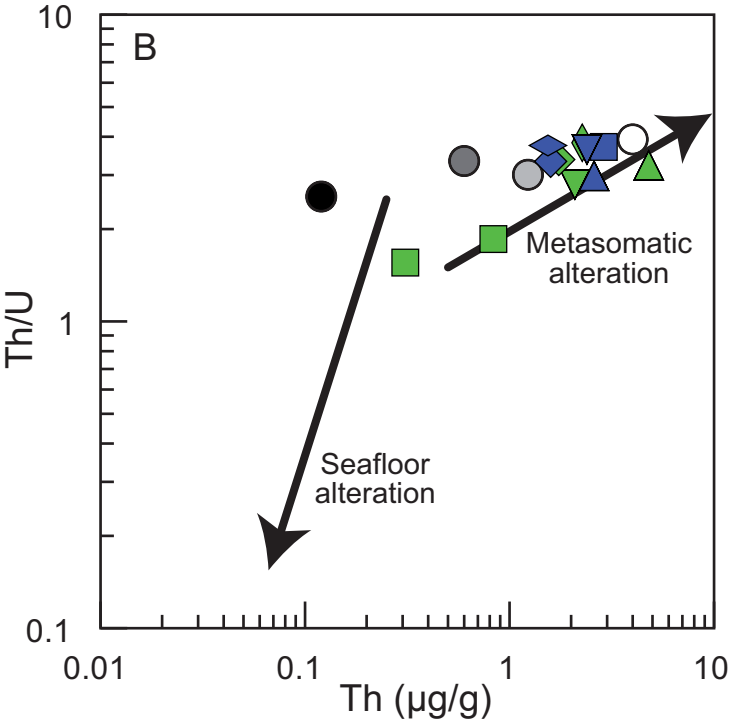
B
Th/U
10
1
0.1
Metasomatic
alteration
Seafloor
alteration
0.01
0.1
1
10
Th (μg/g)

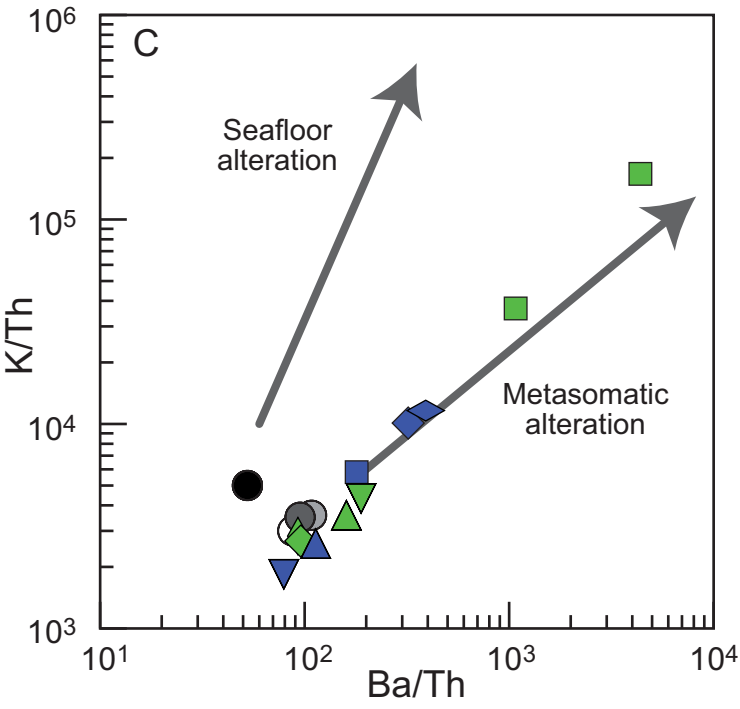
C
K/Th
10^6
10^5
10^4
10^3
Seafloor
alteration
Metasomatic
alteration
10^1
10^2
10^3
10^4
Ba/Th

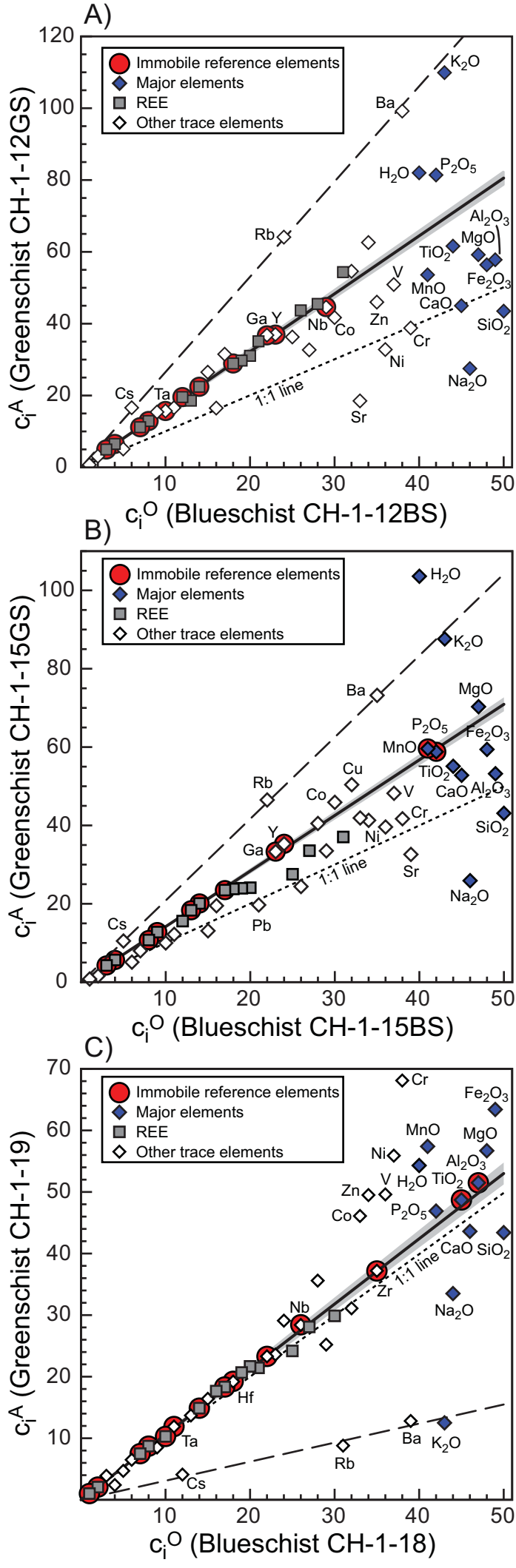
A)
Immobile reference elements
Major elements
REE
Other trace elements
K_2O
Ba
H_2O
P_2O_5
Al_2O_3
MgO
TiO_2
Fe_2O_3
MnO
CaO
SiO_2
Na_2O
Rb
V
Ga
Y
Nb
Co
Zn
Cr
Ni
Cs
Ta
1:1 line
Sr
c_i^A (Greenschist CH-1-12GS)
c_i^O (Blueschist CH-1-12BS)
B)
Immobile reference elements
Major elements
REE
Other trace elements
H_2O
K_2O
Ba
MgO
P_2O_5
Fe_2O_3
MnO
TiO_2
Cu
Rb
Co
V
CaO
Al_2O_3
Cr
SiO_2
Y
Ga
Ni
1:1 line
Sr
Na_2O
Cs
Pb
c_i^A (Greenschist CH-1-15GS)
c_i^O (Blueschist CH-1-15BS)
C)
Immobile reference elements
Major elements
REE
Other trace elements
Cr
Fe_2O_3
MnO
MgO
Ni
Al_2O_3
V
H_2O
TiO_2
Zn
Co
P_2O_5
CaO
SiO_2
1:1 line
Zr
Na_2O
Nb
Hf
Ta
Ba
K_2O
Rb
Cs
c_i^A (Greenschist CH-1-19)
c_i^O (Blueschist CH-1-18)

Fig. 9

Fig. 10

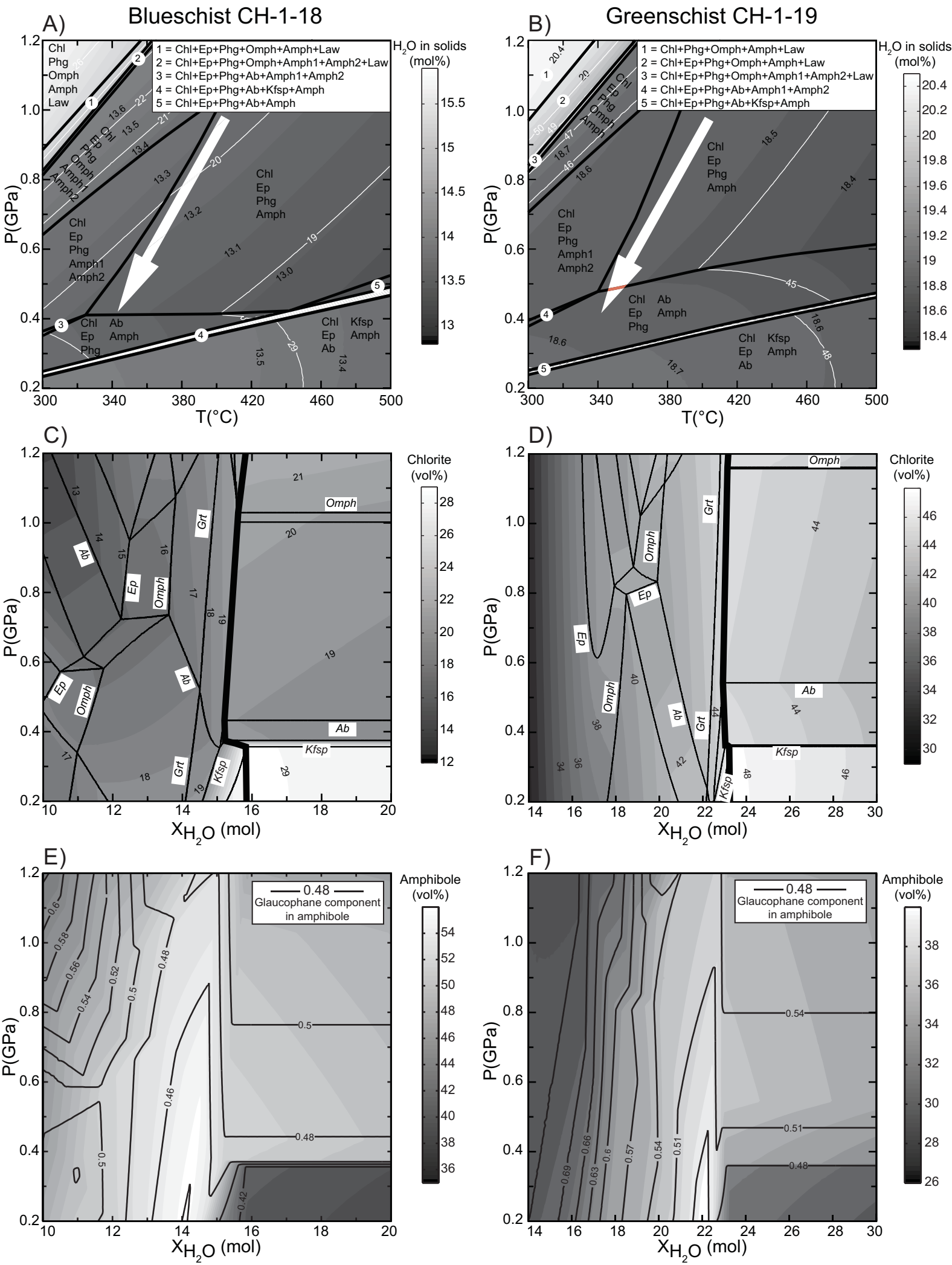
A)
Blueschist CH-1-18
1 = Chl+Ep+Phg+Omph+Amph+Law
2 = Chl+Ep+Phg+Omph+Amph1+Amph2+Law
3 = Chl+Ep+Phg+Ab+Amph1+Amph2
4 = Chl+Ep+Phg+Ab+Kfsp+Amph
5 = Chl+Ep+Phg+Ab+Amph
H2O in solids (mol%)
P(GPa)
T(°C)
B)
Greenschist CH-1-19
1 = Chl+Phg+Omph+Amph+Law
2 = Chl+Ep+Phg+Omph+Amph+Law
3 = Chl+Ep+Phg+Omph+Amph1+Amph2+Law
4 = Chl+Ep+Phg+Ab+Amph1+Amph2
5 = Chl+Ep+Phg+Ab+Kfsp+Amph
H2O in solids (mol%)
P(GPa)
T(°C)
C)
Chlorite (vol%)
P(GPa)
XH2O (mol)
D)
Chlorite (vol%)
P(GPa)
XH2O (mol)
E)
0.48 Glaucophane component in amphibole
Amphibole (vol%)
P(GPa)
XH2O (mol)
F)
0.48 Glaucophane component in amphibole
Amphibole (vol%)
P(GPa)
XH2O (mol)

Fig. 11

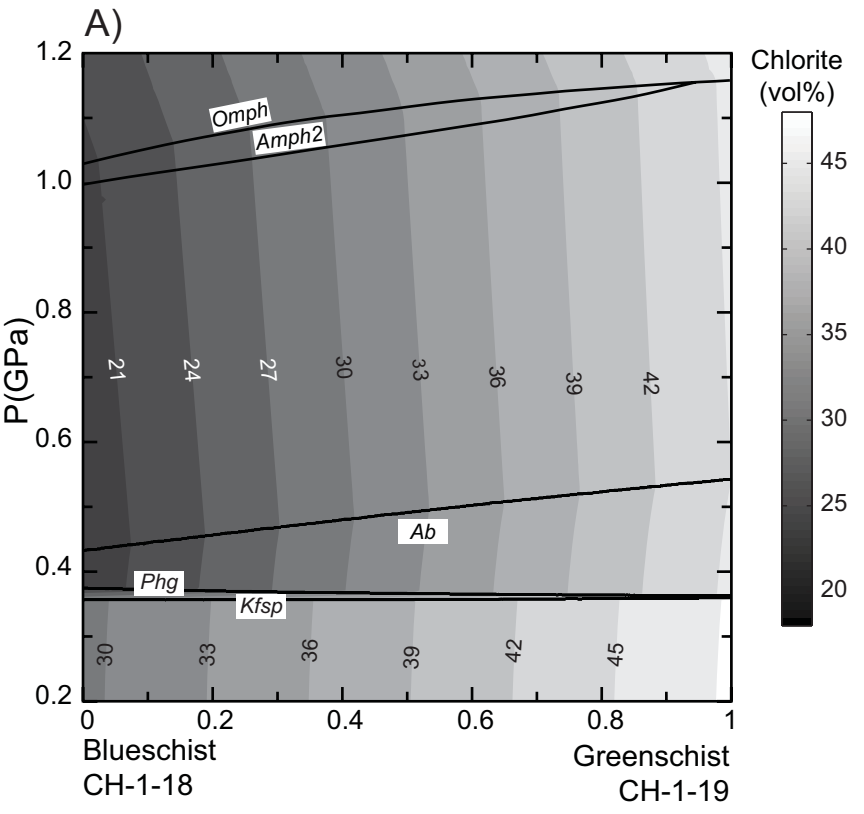
A)
Omph
Amph2
Ab
Phg
Kfsp
21
24
27
30
33
36
39
42
30
33
36
39
42
45
P(GPa)
1.2
1.0
0.8
0.6
0.4
0.2
0
0.2
0.4
0.6
0.8
1
Blueschist
CH-1-18
Greenschist
CH-1-19
Chlorite
(vol%)
45
40
35
30
25
20

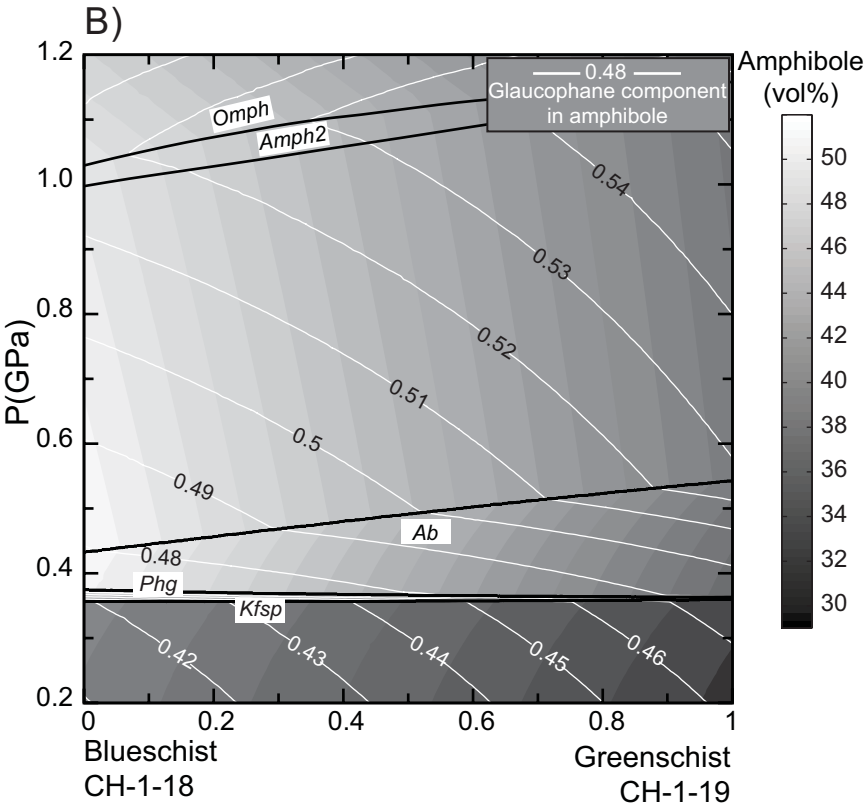
B)
0.48
Glaucophane component
in amphibole
Omph
Amph2
0.54
0.53
0.52
0.51
0.5
0.49
0.48
Ab
Phg
Kfsp
0.42
0.43
0.44
0.45
0.46
P(GPa)
1.2
1.0
0.8
0.6
0.4
0.2
0
0.2
0.4
0.6
0.8
1
Blueschist
CH-1-18
Greenschist
CH-1-19
Amphibole
(vol%)
50
48
46
44
42
40
38
36
34
32
30

Table 1: Whole-rock geochemical analyses of blueschist and greenschist samples from Pichilemu and basaltic reference material BHVO-2.

Rock Type	Greenschist	Blueschist	Greenschist	Blueschist	Blueschist	Blueschist	Blueschist	Blueschist	Greenschist	Greenschist	Greenschist	Blueschist	Greenschist	Basalt	Basalt
Sample	CH 1-12-GS	CH 1-12-BS	CH 1-15GS	CH 1-15BS	CH 1-16	CH 1-18	CH 1-18	CH 1-18	CH 1-19	CH 1-34	CH 1-48A	CH 1-48B	CH 1-48C	BHVO-2	BHVO-2
ICPMS No.	32541	32542	32678	32677	32560	32669	32670	Average	32671	32562	32674	32675	32676	32668	GeoReM*
Major elements (wt.%)															
SiO_2	48.71	56.04	47.87	55.57	47.13			46.48	40.37	43.93	50.08	56.40	52.50		
TiO_2	2.59	1.85	2.43	1.94	2.53			2.55	2.76	2.66	1.19	1.96	1.49		
Al_2O_3	13.50	11.45	12.16	11.21	11.20			11.31	12.39	15.28	15.78	12.24	11.02		
Fe_2O_3	11.70	9.95	12.91	10.44	12.39			12.77	16.53	11.04	11.18	9.54	9.13		
MnO	0.17	0.13	0.16	0.11	0.15			0.15	0.21	0.15	0.13	0.13	0.18		
MgO	8.85	7.03	9.50	6.35	12.24			12.31	14.53	6.00	6.96	5.31	10.76		
CaO	4.90	4.90	6.74	5.74	5.42			5.17	4.90	9.95	2.74	3.26	5.87		
Na_2O	3.43	5.73	3.28	5.82	2.20			2.35	1.79	3.84	1.49	6.06	1.77		
K_2O	2.07	0.81	1.08	0.53	2.15			1.93	0.56	0.77	6.22	2.02	3.68		
P_2O_5	0.31	0.16	0.28	0.20	0.32			0.34	0.38	0.37	0.09	0.16	0.10		
CO_2	n.a	n.a	0.01	0.01	0.02			0.01	0.01	2.95	0.01	0.01	0.01		
H_2O	3.73	1.82	3.73	1.44	3.95			4.28	5.81	3.24	3.77	2.51	2.95		
Total	**99.96**	**99.87**	**100.15**	**99.36**	**99.70**			**99.65**	**100.24**	**100.18**	**99.64**	**99.60**	**99.46**		
Trace elements (µg/g)															
Li	28.6	19.7	28.6	24.8	53.1	44.1	44.2	44.2	56.1	26.8	25.2	34.2	21.9	4.43	4.8±0.2
Sc	27.4	22.6	34.6	23.9	18.8	19.0	19.1	19.0	19.5	27.6	32.0	22.1	27.4	31.2	32±1
V	315	229	320	246	304	304	306	305	284	300	335	210	215	330	317±11
Cr	380	382	566	516	496	468	475	472	845	80.9	539	460	734	291	280±19
Co	52.0	37.5	58.2	38.1	62.3	64.0	64.4	64.2	89.8	38.7	51.5	45.4	44.0	44.3	45±3
Ni	199	218	218	198	262	253	254	254	383	60.6	272	285	245	119	119±7
Cu	110	64.4	127	80.9	45.7	45.3	45.1	45.2	39.3	85.9	108	158	216	125	127±7
Zn	135	102	127	99.7	104	110	111	110	161	85.9	75.6	87.4	102	105	103±6
Ga	25.0	15.0	21.6	14.9	18.6	19.1	19.2	19.1	23.2	21.2	21.4	12.5	16.7	21.1	22±2
Rb	52.3	19.6	28.2	13.3	51.4	47.4	47.4	47.4	13.4	17.5	164	51.7	90.5	9.04	9.11±0.04
Sr	40.8	72.5	486	582	54.3	50.1	50.1	50.1	48.6	681	22.5	42.8	25.6	397	396±1
Y	29.1	18.1	28.5	19.3	15.9	16.6	16.7	16.6	17.6	19.0	17.0	23.2	17.8	25.0	26±2
Zr	172	93.5	176	145	141	194	194	194	206	104	65.0	168	98.7	175	172±11
Nb	36.5	23.7	22.3	23.7	23.6	24.1	24.1	24.1	26.3	37.9	3.70	21.9	8.88	17.8	18.1±1
Mo	0.080	0.108	0.074	0.088	0.372	0.275	0.284	0.280	0.168	0.088	0.162	0.286	0.057	5.68	4±0.2
Sn	2.14	1.42	1.64	1.48	1.61	1.55	1.57	1.56	1.64	1.53	0.726	1.66	1.05	1.69	1.7±0.2
Sb	0.411	0.401	0.430	0.502	0.348	0.340	0.341	0.340	0.323	0.343	0.202	0.275	0.399	0.094	0.13±0.4
Cs	1.57	0.565	0.853	0.407	1.73	1.50	1.51	1.50	0.508	0.846	4.83	1.43	2.75	0.087	0.1±0.01
Ba	765	293	394	189	603	504	515	510	167	217	1356	519	896	134	131±1
La	34.1	20.3	22.3	20.2	19.2	20.3	20.3	20.3	19.6	23.8	3.60	21.0	8.87	15.9	15.2±0.1
Ce	78.1	44.6	54.4	45.5	45.5	47.0	46.9	47.0	46.8	50.9	8.98	56.9	23.0	39.3	37.5±0.2
Pr	9.21	5.51	6.80	5.65	6.21	6.39	6.37	6.38	6.51	6.52	1.47	6.39	3.18	5.62	5.35±0.17
Nd	36.9	22.7	29.5	23.7	27.2	27.8	27.8	27.8	28.9	27.5	7.58	27.0	14.5	25.8	24.5±0.1
Sm	7.87	5.07	6.88	5.46	6.22	6.27	6.30	6.28	6.81	6.08	2.51	6.23	3.81	6.41	6.07±0.01
Eu	2.28	1.60	2.21	1.70	2.00	2.03	2.04	2.04	2.25	2.04	0.951	1.93	1.27	2.16	2.07±0.02
Gd	7.65	4.89	7.04	5.33	5.82	5.85	5.86	5.85	6.37	5.86	3.16	6.12	4.13	6.52	6.24±0.03
Tb	1.17	0.732	1.07	0.798	0.794	0.802	0.804	0.803	0.875	0.844	0.544	0.935	0.655	0.982	0.92±0.03
Dy	6.67	4.15	6.23	4.51	4.03	4.04	4.10	4.07	4.39	4.52	3.47	5.36	3.90	5.57	5.31±0.02
Ho	1.23	0.765	1.17	0.825	0.657	0.672	0.676	0.674	0.722	0.786	0.694	1.01	0.746	1.02	0.98±0.04
Er	3.10	1.94	3.03	2.11	1.48	1.57	1.59	1.58	1.68	1.85	1.84	2.62	1.94	2.56	2.54±0.01
Tm	0.414	0.254	0.411	0.290	0.179	0.201	0.198	0.199	0.206	0.230	0.262	0.370	0.270	0.339	0.33±0.01
Yb	2.49	1.53	2.60	1.84	1.03	1.20	1.20	1.20	1.24	1.30	1.66	2.40	1.74	2.09	2±0.01
Lu	0.323	0.195	0.366	0.258	0.129	0.164	0.165	0.164	0.167	0.158	0.231	0.342	0.245	0.286	0.274±0.005
Hf	3.87	2.19	4.15	3.42	3.07	4.30	4.32	4.31	4.61	2.56	1.71	3.82	2.51	4.43	4.36±0.14
Ta	2.07	1.32	1.27	1.26	1.36	1.36	1.38	1.37	1.48	2.13	0.20	1.27	0.48	1.07	1.14±0.06
W	0.229	0.149	0.151	0.185	0.267	0.237	0.245	0.241	0.313	0.269	0.259	0.169	0.183	0.244	0.21±0.11
Pb	2.40	2.32	5.45	5.82	1.65	1.17	1.15	1.16	1.10	3.27	1.31	1.82	1.46	1.78	1.6±0.3
Th	4.79	2.59	2.09	2.39	1.54	1.60	1.57	1.59	1.74	2.39	0.31	2.89	0.83	1.19	1.22±0.06
U	1.49	0.869	0.747	0.658	0.411	0.483	0.473	0.478	0.517	0.620	0.199	0.780	0.449	0.412	0.403±0.001

n.a. = not analyzed

* GeoReM preferred values (http://georem.mpch-mainz.gwdg.de/) are given for comparison

Table 2: Modal mineral proportions of three selected blueschist-greenschist pairs

Sample	Sodic amphibole	Sodic-calcic & calcic amphibole	Phengite	Chlorite	Albite	Titanite	Epidote	Alkali feldspar	Hematite	Apatite	Other phases (<<1%)
CH 1-18 BS	12	22	25	7	20	8	3	–	3	<1	zircon
CH 1-19 GS	1	21	10	37	20	9	<1	1	<1	1	
CH 1-12 BS	10	39	2	11	28	6	2	2	<1	<1	zircon, rutile
CH 1-12 GS	3	37	9	20	24	5	–	2	<1	<1	
CH 1-15 BS	16	24	4	10	34	3	8	–	1	<1	
CH 1-15 GS	3	39	3	23	22	1	5	<1	2	2	

Mineral proportions of each sample were estimated based on several representative BSE images